Politecnico di Torino
Master's Degree in Nanotechnologies for ICTs

Master Degree Thesis

Magnetoelectric devices for beyond CMOS applications

Supervisors:

Dr. Christoph Adelmann
Dr. Florin Ciubotaru
Prof. Marco Vacca

Candidate:

Francesco Privizzini

Academic Year 2023/2024

Abstract

The Moore's law has led the pace of innovation predicting an exponential growth in computing unit performances. However, as the dimensional and functional scaling of CMOS technologies approaches fundamental limits, the search for alternatives solutions has intensified. Spintronics emerges as a promising field among the so called beyond-CMOS technologies, manipulating the spins of electrons for different applications such as logic. Anyway, to best integrate this technology, spintronics needs the development of scalable and energy-efficient devices and an in-depth study of the magnetic materials used. In this context, this thesis studies some magnetoelectric devices made by composite form by thin piezoelectric and magnetostrictive layers aiming to quantify the magnetoelectric effect, which could be relevant for future spintronics applications. These devices are investigated using anisotropic magnetoresistance measurements, with a primary focus in the understanding of the magnetoelectric coupling in these novel structures with various configurations and to examine the magnetic properties of the magnetostrictive layer. They are characterized by the ability to modulate the electrical resistance in response to changes in the angle between the direction of the electric current and the orientation of the magnetization within the material. The magnetoelectric effect, which involves the coupling of electric fields to intrinsic magnetization, presents a viable pathway for this low-power and controlled magnetization switching. This coupling is facilitated by the bilayer structure of piezoelectric and magnetostrictive thin films of these structures, where strain induced in the piezoelectric layer by an applied electric field is transferred to the magnetostrictive layer, thereby switching its magnetization. The study emphasizes the use of nickel as the main material, while also briefly incorporating Cobalt-Iron-Boron research as a comparison. Once the parameters are known, it is important to study how the device reacts under the effect of a magnetic and electric field. Hence the experimental data obtained in cleanroom has been compared with the results gotten by performing some simulations. Having several physical phenomena involved, COMSOL has been used for the study of the distribution of the strain in the nanostrip. On the other hand Mumax3, a GPU-accelerated micromagnetic simulation program, has been used to perform micromagnetic simulations and OOMMF to visualize the magnetic moments and domains. Simulations show how the device design is appropriate to achieve uniform strain at the centre of the strip while the coercivity, thus the ease of manipulating the magnetic domains, depends strongly on the size. Furthermore the response of the magnetization versus voltage has been measured showing that the magnetoelec-

tric effect exists in such devices. The devices respond very well by applying small voltages, but the smaller the size of the nanostrip, the lower the maximum voltage that can be withstood. Indeed experimental data are coherent with the simulations showing that magnetization can be rotated using magnetoelectric effect although further measurements need to be made in order to get a more accurate value of coupling. In conclusion further research and enhancement are briefly discussed for improving device efficiency and magnetoelectric coupling coefficient.

List of Figures

List of Tables

Contents

Chapter 1

Introduction

In the area of semiconductor technology, Moore's Law has long guided the relentless pace of innovation, predicting a doubling in transistor density roughly every two years. This scaling has led to an era of smaller, faster, and more cost-effective integrated circuits [1], enabling profound advancements across diverse applications. However as CMOS technology's dimensional and functional scalability gets closer to its basic constraints [2], the semiconductor industry faces escalating challenges in maintaining this trajectory. These challenges include improving performance, managing heat and reducing power dissipation. These limitations have prompted extensive research into novel information processing and memory devices, microarchitectures, and system paradigms, as stated in recent roadmaps. This interest in innovation gave rise to the concept of *Beyond CMOS technologies*.

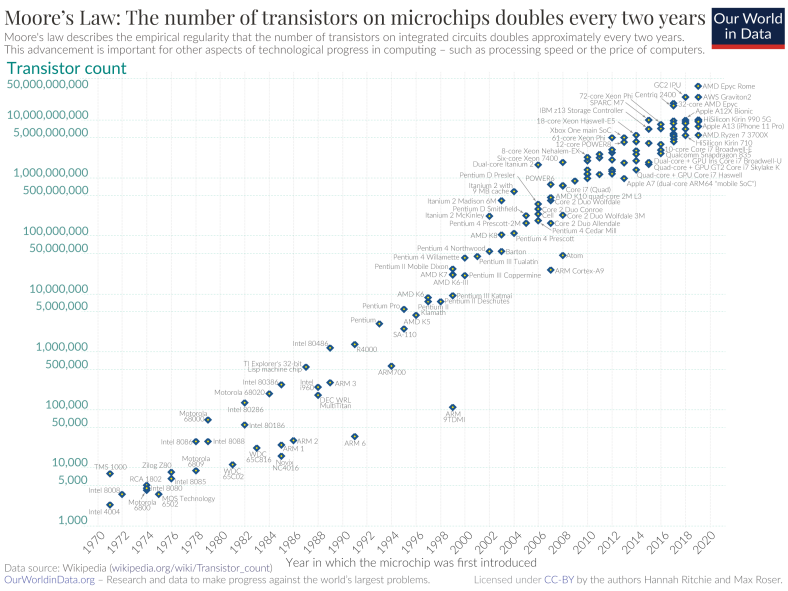

Figure 1.1: Moore's Law showing the timeline of transistor counts in microchips between 1970 and 2020. [3]

The term beyond CMOS describes future advancements in digital logic technol-

ogy that will surpass the present scaling constraints of CMOS. The goal of these developments is not only to reduce the impacts of heat but also to maintain the same device density and performance as the current semiconductor electronics by reducing power dissipation [2].

Spintronics, which offers new avenues for information processing through the active manipulation and control of electron spin inside solid-state systems [4], is one of the most promising areas of this research.

Magnetoelectric devices are one of the numerous concepts in the field of spintronics that have gained attention recently due to their potential.

These devices are unique in that they can couple electrical and magnetic properties, which allows one to regulate the magnetization process by using an electric field.

These devices have a great deal of potential; in fact, their application may result in the creation of energy-efficient magnetic memory devices [11] [13], wireless sensor networks [13], magnetoelectric sensor [8] or ultralow power logic devices [10].

Recently, new device concepts have been developed, such as the Magneto Electric Spin Orbit (MESO) logic [5] or magnetoelectric RAM [7] where the application of a voltage can modulate the interaction between ferromagnetic magnetic and multiferroic layers in the system. The latter are a special class of materials with more than one ferroic order [10] at the same time.

In any case, the use of multiferroics is not ideal. Since Coulomb forces are much greater than magnetic forces [12], the coupling between ferroelectric and ferromagnetic properties is small in these materials. They should also be used at cryogenic temperatures to take advantage of their magnetic properties [11].

Composites could provide a solution to these problems. In these devices, there is the ability to bind the properties of one layer to another. The great potential of composites is to be able to choose materials according to their properties in order to tailor the desired characteristics. Furthermore, being based on known materials, they have the high potential to be miniaturised in order to be integrated with current technology [9]. This miniaturization could as well lead to the realization of new and efficient devices useful in various applications. One example is wireless power transducers that can be used in the biomedical field [6].

In this thesis, the devices studied couple electrical and magnetic properties through mechanical forces. To maximize the magnetoelectric effect, it is essential to understand the properties of the thin film layers involved and the manufacturing procedures. The study in this thesis focuses on the use of the anisotropic magnetoresistance (AMR) effect to quantify the coupling. AMR devices are characterized by their ability to modulate electrical resistance in response to changes in the angle between the direction of the electric current and the orientation of the magnetization within the material. Once the parameters are known, it is important to study the magnet's behavior in both magnetic and electric fields, understand the effects of different parameters, such as coercivity and geometry, on the magnetic properties and figure out how to maximize the coupling.

Chapter 2

Theoretical concepts

2.1 Magnetism

Magnetic effects are entirely quantum mechanical phenomena, as they are mainly caused by the motion and the spin of electrons. However, while classical explanations can be used initially, quantum mechanics will be needed to fully explain the physics of the devices.

Considering initially Bohr's atomic model, an electron circulating around the nucleus with an orbit of radius r generates a circular current I_e, which consequently creates a magnetic dipole moment $\mu_d = I_e \pi r^2$ perpendicular to the orbital plane. The nucleus in turn exerts a force on the electron, which results in the generation of an angular momentum $L = m_e r^2 \omega$.
Hence for a single electron, it is possible to obtain the following relation given by the *gyromagnetic ratio* γ, such that:

$$\mu_L = \gamma L = -\frac{e}{2m_e} L \tag{2.1}$$

where e represents the electron's charge and m_e is its mass.
Equation 2.1 is valid for orbital motion but electrons also have spin, which is their rotation around their own axis. Moreover in quantum mechanics, the energy levels of an atom are discrete, so both the angular momentum and the magnetic dipole are quantized in units of $\hbar$. Then it is possible to find the magnetic moment relative to the spin angular momentum S:

$$\mu_s = -\frac{g_s \mu_B}{\hbar} S \tag{2.2}$$

where g is called *Landé* or *g-factor* and $\mu_B = \frac{e\hbar}{2m_e}$, the *Bohr magneton*, represents the smallest dipole momentum of an electron. For a pure orbital moment, the g-factor is 1, and for a pure spin moment, it is 2. However, in complex systems, it may be any other number in between. Typically, in any atom, the sum of the orbital and spin rotations of several electrons generates the total angular momentum. The Russel-Saunders coupling theorem states that the total magnetic moment is equal to the

sum of the contributions from the orbital and spin angular momentum when their interaction is weak. A different formula is used to find the total magnetic moment of an electron when the interaction between spin and orbital angular momentum becomes important and cannot be ignored. Therefore the previous equation is corrected to:

$$\mu = \frac{g\mu_B}{\hbar} J = -g\frac{e}{2m_e} J = -\frac{e}{2m_e}(g_L L + g_S S) \tag{2.3}$$

where J is the total angular momentum, it is possible to obtain the general expression of the *Landé factor* g starting from 2.3, multiplying first and second members by J we get:

$$\mu J = \frac{\mu_B}{\hbar}(g_L LJ + g_S SJ) = \frac{g\mu_B}{\hbar} J^2 \tag{2.4}$$

Since $J = L + S$:

$$L^2 = (J - S)^2 = J^2 + S^2 - 2SJ \xrightarrow{\text{thus}} SJ = \frac{1}{2}(J^2 + S^2 - L^2) \tag{2.5}$$

In the same way it is possible to calculate:

$$LJ = \frac{1}{2}(J^2 + L^2 - S^2) \tag{2.6}$$

Inserting 2.6 and 2.5 into 2.4 and assuming $g_L = 1$ and $g_S = 2$ the *g-factor* is expressed by:

$$g = \frac{3}{2} + \frac{S^2 - L^2}{2J^2} \tag{2.7}$$

Since all this holds for a single electron, the sum of the magnetic moments of an atom's electrons will determine its overall magnetic moment. Thus, the total angular momentum of full electron shells will be zero. On the other hand, magnetic effects can arise and the spin and orbital angular momentum of an atom can diverge from zero if its electrons are in empty shells. Using the same logic, the total magnetic moment is equal to the sum of the total magnetic moments of all the atoms in a sample. In this context, the magnetization vector is defined as the sum of all the magnetic moments per unit volume:

$$M = \frac{\sum_i \sum_j \mu_{ij}}{\delta V} \tag{2.8}$$

where i and j are the number of atoms and valence electrons respectively.

2.2 Magnetic interactions

The long-range interactions between magnetic moments in a material are called magnetic interactions. Indeed, many properties based on the fact that magnetic moments feel others next to them are due to these interactions. Their main consequence is the generation of forces used to minimize the energy of the system. As

a result, they are only quantum-mechanical because they affect the configuration of atomic spin. How the system's energy is minimized, and consequently the magnetization as well, depends on a number of parameters. These parameters can be categorized as either non-local or in-local. Anisotropy energy, exchange energy and magnetoelastic contribution are examples of in-local. Examples of non-local contributions brought about by differences in the direction of magnetization of different sample sections are the dipolar and the magnetostrictive term [14].

2.2.1 Exchange interactions

Exchange interactions can be defined as the tendency of a magnetic material to favor the alignment of adjacent spins parallel or antiparallel to each other [15]. It is a quantum-mechanical phenomenon that depends on both Coulomb interactions and the Pauli exclusion principle. Indeed the origin of this interaction is due to *exchange forces* caused by the orientation of the spins of two different electrons in a system. When the spins are antiparallel, the molecule is stable. On the other hand, when the spins are parallel electrons tend to repel one another, and so the ordinary Coulomb electrostatic energy is changed as well. For a many-electron system, the interaction between two adjacent spins, S_i and S_j, can be represented by the Hamiltonian:

$$E_{ex} = -2\sum_{j\neq i}^{N} \mathcal{J}_{ij} S_i \cdot S_j \tag{2.9}$$

where $\mathcal{J}$ is a specific integral that appears in the exchange effect calculation and is referred to as the exchange integral. At first glance, it is interesting to note that this forces are primarily influenced by the distances between atoms rather than the geometrical arrangement of their positions. As a result, also amorphous material can exhibit ferromagnetism. Moving to a macroscopic view, it is possible to obtain a formula that expresses the energy per unit volume of this interaction as a function of magnetization such as:

$$E_{ex} = A_{ex}(\nabla m)^2 \tag{2.10}$$

A_{ex} is the *exchange stiffness* and it is defined as:

$$A_{\text{ex}} = \frac{n\mathcal{J}S^2}{a} \tag{2.11}$$

where n is the the number of atoms in a unit cell and a is the crystal lattice parameter of the material. It is an important parameter to take into account mainly in the simulations because it quantifies the extent to which the magnetization tends to align with the surrounding magnetization. To get the value of the effective field the following simple definition has to be applied:

$$H_{eff} = -\frac{1}{\mu_0 M_s}\frac{\partial E}{\partial m} \tag{2.12}$$

where μ_0 is the vacuum permeability. In this way the effective exchange field will be:

$$H_{ex} = -\frac{2}{\mu_0 M_s} A_{ex} \Delta m \tag{2.13}$$

In addition, the *exchange length*, which is another very important parameter for simulations, can be obtained from A_{ex} as:

$$l_{ex} = \sqrt{\frac{2A_{ex}}{\mu_0 M_s^2}} \tag{2.14}$$

This length represents the range across which the magnetization is likely to vary. Given that abrupt changes in magnetization require more energy, it makes natural that this length increases with exchange stiffness.

2.2.2 Zeeman energy

The potential energy of a magnetized body in an external magnetic field is known as Zeeman energy [16]. It is given by:

$$E_Z = -\mu_0 M \cdot H_{ext} \tag{2.15}$$

This indicates that in order to minimize the Zeeman energy and so reach a stable state, the magnetic dipoles tend to be parallel with the external magnetic field H_{ext}.

2.2.3 Magnetostatic interactions

Magnetostatic interactions are due to the interaction among the magnetic moments around of the other elements of the volume in the magnets. This kind of interaction is described by using the so called *demagnetization field* H_{dem} which tends to minimize the overall energy of the system. This field is given by:

$$\nabla \cdot B = \mu_0 \nabla (H + M) = 0 \rightarrow \nabla H_{dem} = -\nabla M \tag{2.16}$$

Knowing the demagnetization field, the magnetostatic energy can be easily derived as:

$$E_{MS} = -\frac{1}{2}\mu_0 \int H_{dem} \cdot M dV \tag{2.17}$$

Generally H_{dem} is strongly dependent on the shape and aspect ratio of the sample. The simplest scenarios to study are that of thin films or ellipsoid, for which the demagnetization field is:

$$H_{dem} = -N_D M \tag{2.18}$$

where N_D is the *demagnetization tensor* and its trace is one for the above mentioned cases. In all the other situations the evaluation of N_D is not trivial because it results not constant throughout the volume.

2.2.4 Anisotropy

As mentioned before, the geometry and even the nature of the magnet play a significant role on the direction of magnetization and consequently on the response to external stimuli. This dependence is called *magnetic anisotropy* and it may come from several intrinsic factors. So, especially in thin films, it is more convenient express the magnetic anisotropy using the *effective anisotropy constant* K_{eff} given by the sum of all the contributions. The most relevant factors are:

- **magnetocrystalline anistropy** due to the spin orbit interaction of electrons [23]. The crystallographic structure is correlated with the orbital symmetry of the valence electrons thus with their orbital momentum. As shown in 2.3, the spin angular momentum is linked with the orbital momentum therefore it is linked to the symmetry of the crystal as well. For the work done in this thesis, this contribution is actually negligible having mostly had to deal with polycrystalline and amorphous materials in which the contributions explained below are most relevant;

- **shape anistropy** which represents the magnetostatic contribution given by the demagnetization field. Hence it arises from dipole-dipole interactions that are influenced by shape and the size as seen before.

- **magnetoelastic anisotropy** that can occur in two different ways, one the reverse of the other:

  1. the application of a magnetic field can stretch or contract the material due to the movement of internal magnetic domains that align with the direction of the applied field, as shown in Figure 2.1. This effect is know as *magnetostriction effect* or *Joule effect*.
  2. Vice versa, the application of a strain can change its magnetization. This happens because in general strain modifies the distance between the atomic dipoles, leading to a change in the exchange and dipolar energies. This effect is called *inverse magnetostriction effect* or *Villari effect*.

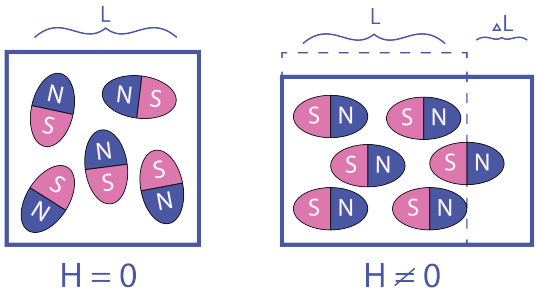

Figure 2.1: Illustration of the magnetostriction effect

The magnetoelastic anisotropy expresson is:

$$K_{me} = \frac{3}{2}\lambda_s \sigma \tag{2.19}$$

where λ_s is the *saturation magnetostriction* and σ is the stress acting on the film [14]. By analyzing the parameters involved, it becomes clear the role played by this factor in the behavior of the devices studied in this thesis. The choice of λ_s and σ are very important for the management of magnetization and related device properties. The interaction between strain and magnetization is described by the *magnetoelastic energy* defined as:

$$\begin{aligned} E_{me} = B_1 \left[\left(m_x^2 - \tfrac{1}{3}\right) \epsilon_{xx} + \left(m_y^2 - \tfrac{1}{3}\right) \epsilon_{yy} + \left(m_z^2 - \tfrac{1}{3}\right) \epsilon_{zz} \right] \\ + B_2 \left(m_x m_y \epsilon_{xy} + m_y m_z \epsilon_{yz} + m_x m_z \epsilon_{xz}\right) \end{aligned} \tag{2.20}$$

where:

- $m_{x,y,z}$ are the normalized magnetization coefficients;
- ϵ_{xx}, ϵ_{yy}, ϵ_{zz} are the normal elements of the strain tensor;
- ϵ_{xy}, ϵ_{yz}, ϵ_{xz} are the shear elements of the strain tensor;
- B_1 and B_2 are the *magnetoelastic coupling coefficients* which are a measure of the strength of the strain-dependent terms. The magnetostriction coefficient and the magnetoelastic coupling coefficient are directly related to each other by elastic constants:

$$B_1 = \tfrac{3}{2}\lambda_{100}(c_{12} - c_{11}) \quad B_2 = -3\lambda_{111} c_{44} \tag{2.21}$$

Now it is important to find the value of the effective field using 2.12 by getting:

$$H_{me} = -\frac{2}{\mu_0 M_s} \begin{pmatrix} B_1 m_x \epsilon_{xx} + B_2(m_y \epsilon_{xy} + m_z \epsilon_{zx}) \\ B_1 m_y \epsilon_{yy} + B_2(m_x \epsilon_{xy} + m_z \epsilon_{yz}) \\ B_1 m_z \epsilon_{zz} + B_2(m_x \epsilon_{xz} + m_y \epsilon_{yz}) \end{pmatrix} \tag{2.22}$$

2.3 The Landau-Lifshitz-Gilbert equation

Once all the energies related to the various interactions have been obtained and 2.12 applied to obtain the effective field related to that particular phenomenon, it is sufficient to sum each contribute to obtain the effective field that the magnet feels:

$$H_{eff} = H_{ex} + H_{ext} + H_{dem} + H_{me} \tag{2.23}$$

For completeness but especially to understand how mumax3 works, it is appropriate introduce that equation that describes the dynamics of magnetization. Considering for simplicity a single magnetic dipole interacting with the effective magnetic field, if the angle between the two vector is not zero the magnetization starts to change over the time. This change is caused by the torque defined as:

$$\tau = \mu_0(\mu \times H_{eff}) \tag{2.24}$$

This torque is perpendicular to both μ and H_{eff} leading to a precessional movement of the magnetization around the effective magnetic field. By definition the torque is also the gradient of the angular momentum with respect to time:

$$\tau = \frac{dJ}{dt} \tag{2.25}$$

Hence using as angular momentum the expression obtained in 2.3 and combining 2.25 with 2.24 it is possible to get an equation which describes the change of magnetization over time:

$$\frac{d\mu}{dt} = \gamma_{LLG}(\mu \times H_{eff}) \tag{2.26}$$

where $\gamma_{LLG} = -\mu_0 g \frac{e}{2m_e}$ is called *Landau-Lifshitz gyromagnetic ratio*. This equation is not complete because it doesn't consider any damping. Moreover it takes into account only the movement of a dipole. Moving over the entire volume of the structure and considering the dissipation terms the complete *Landau-Lifshitz-Gilbert equation* is obtained:

$$\frac{dM}{dt} = \gamma_{LLG}(\mu \times H_{eff}) + \frac{\alpha}{M_S}\left(M \times \frac{dM}{dt}\right) \tag{2.27}$$

where α is a phenomenological constant called *Gilbert damping* which collects all the effects due to the dissipation. With the introduction of the damping term, the path traced by the magnetization around H_{eff} becomes non circular. Instead the magnetization vector spirals towards the magnetic field until it becomes fully aligned.

2.4 Ferromagnetism

Ferromagnetism is the property of some materials, generally transition metals and alloy of rare-earth metals, characterized by a spontaneous magnetization even in the absence of an external magnetic field. Above a certain temperature called *Curie temperature* T_C the spontaneous magnetization vanishes making that material paramagnetic. In the demagnetized state, a ferromagnetic material is partitioned into several small regions known as *domains* in which all the moments have the same orientation. Each domain is inherently magnetized to the saturation value M_S, which depends on the material, but for different domains the direction of magnetization is arranged such that the overall specimen has zero net magnetization. When an external magnetic field is applied, the process of magnetization occurs converting the specimen from a multi-domain state into a single-domain state magnetized towards the direction of the applied field [22]. The boundary where the direction of magnetization changes from one domain to the next is called *domain wall*. One consequence of switching magnetic domains in ferromagnets is the presence of hysteresis loop, as illustrated in Figure 2.2.

This happens because the magnetic domains do not always respond in the same way in the presence of the same magnetic field due to the interaction of the domains with the impurities and imperfections of the material. In fact, material imperfections put disorder in the system by going on to change the coupling between the local moments and the surroundings accordingly. For this reason, the magnetization at any given moment depends not only on the value of the applied magnetic field but also on its past value. Important information about the material can be extracted from the hysteresis loop. First of all, the remanence when no field is applied, the coercivity which is the magnetic field value to be applied to cancel to cancel the magnetization. This value is very important because it also indicates the difficulty to magnetize a material. A material with a low coercivity (less than or equal to $5 \times 10^3 A/m$ [15]) is called "$soft$" and interact with weak magnetic fields, otherwise it is called "$hard$". Dealing with thin films, it is clear that a variety of factors, including temperature, sample geometry, impurity concentration, and applied magnetic field direction, will have the greatest influence on the hysteretic cycle's shape and on the values of parameters like permeability and coercivity. When examining a thin-film sample, for instance, the presence of different anisotropies causes the domains to preferentially arrange themselves along certain orientations, or *easy axes*, rather than in any other directions. A hysteresis loop resembling the one in Figure 2.2 can be created by applying a longitudinal magnetic field with respect to the easy axis.

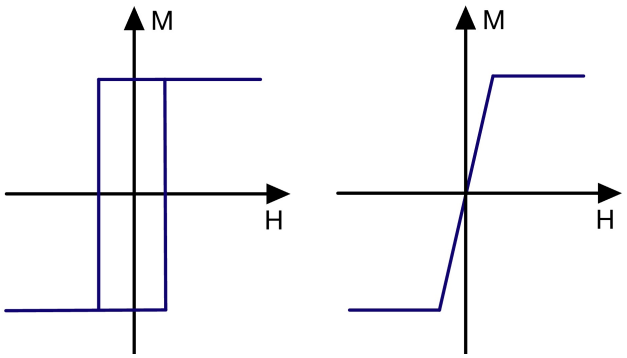

Figure 2.2: Theoretical hysteresis loops for a soft magnetic material in the longitudinal direction (left) and in the transverse direction (right) with respect to the easy axis

2.4.1 Anisotropic magnetoresistance

To understand in detail how the studied devices work, it is appropriate to understand why changing a magnetic field changes the resistance of a sample accordingly. In a transition metal such as nickel, the outermost electronic shells are the 4s and 3d, which are very different. As shown in Figure 2.3, the 4s band has a lower density of states and is full of electrons having opposite spins. In contrast, the narrow 3d has a much higher density of states, so the electron mobility is much lower than the electrons in 4s, and it has more free states. In addition, the 3d orbital not be-

ing completely full has a number of spin-up electrons different from the spin-down electron that divide the band into two spin-split bands [31]. The magnetic moment will appear mainly to the electron in 3d bands while the material current will be given by the electrons in 4s with higher mobility.

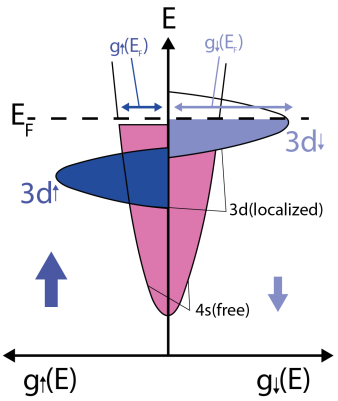

Figure 2.3: Density of states (DOS) in a ferromagnetic metal showing the differences between spin-up and spin-down electrons

The resistivity of a body is always related to scattering mechanisms that cause transitions between individual particle states. In the case of transition metals by applying an external magnetic field, electrons from the 4s (with lower DOS) will go into the 3d spin-split (with higher DOS). The increase in the number of electrons with having the same spin in the 3d band causes the resistance to increase.

According to Mott's model, electrons with opposite spins do not mix, so assuming we are at low temperatures thus ignoring magnon scattering, two independent currents flow inside a body, one with spin up and one with spin down.

Electrons with majority spin that travel parallel to the direction of magnetization have the highest probability of scattering [18]. For this reason, when magnetization and current are parallel the resistance is maximum, while when they are perpendicular we have minimum resistance. Therefore, AMR is defined as the sample resistance's change with the magnetization's orientation with respect to the applied electric current's direction [19], which can be described by the following equation:

$$\rho = \rho_{\perp} + (\rho_{\parallel} - \rho_{\perp}) cos^2(\theta_M) \tag{2.28}$$

where θ_M is the angle between the direction of the magnetization and the current flow, $\rho_{\parallel}$ and $\rho_{\perp}$ are the resistance at $\theta_M = 0°$ and $\theta_M = 90°$ respectively [20].

2.5 Piezoelectricity

Piezoelectricity is the property of some dielectric materials that manifests itself in two different effects, one the opposite of the other:

- when the body is subjected to mechanical stress it polarizes with a polarization proportional to the stress applied. This happens because the stress changes the crystal's structure by reorienting the electric dipoles. In this case we speak of *direct piezoelectric effect* and the coefficient that best describes this link is the *g-coefficient* defined as the ratio between the voltage per mechanical stress.

- when the body becomes strained as a result of an electric field application. Once again, the electric field causes the electric dipoles of the material to move, generating stress. In this case the effect is called *reverse or indirect piezoelectric effect* and *d-coefficient* is the ratio between the strain and the applied voltage/electric field.

Piezoelectric materials can also be ferroelectric. In ferroelectric materials, nonlinear polarization behavior includes hysteresis and saturation at high applied electric fields One important feature of ferroelectric piezoelectric materials' behavior in an electric field is the butterfly loop phenomenon shown in Figure 2.4. Therefore, understanding is necessary to maximize the performance of piezoelectric materials in a variety of fields, including magnetoelectric applications. The strain in the piezoelectric material initially grows practically linearly with the electric field (voltage), reaching a maximum strain constrained by the material's polarization saturation. The strain drops when the electric field is reduced, albeit more slowly than the electric field. The rate of strain reduction increases as the electric field gets smaller. Subsequently, the material experiences a sudden shift in polarity and an increase in strain until it approaches its physical limit under negative voltage. At this crucial moment, the material's polarization is totally reversed. As the electric field reverses and becomes positive again, the strain initially decreases at a slower rate than the electric field. But again, the rate of strain reduction increases as the electric field decreases. Eventually, the material reaches another critical point where it abruptly changes polarity, leading to an expansion until it hits its physical limit again.

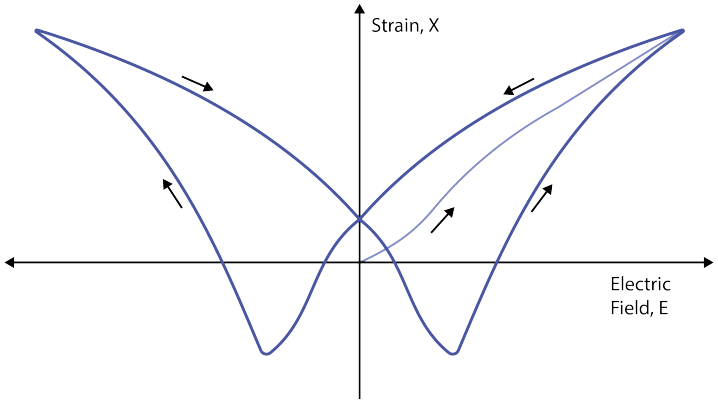

Figure 2.4: Illustration of Strain versus electric field loop (butterfly loop) in a ferroelectric material

2.6 Magnetoelectric effect

As said in the previous paragraphs, magnetoelectricity is a phenomenon that refers to the coupling between magnetic and electric fields in matter, allowing the control of magnetic properties through an electric field and vice versa. Composites composed of ferromagnetic and ferroelectric phases also exhibit magnetoelectric behavior. The device studied in this thesis use strain to couple the two different phases. In detail when these composites are exposed to an electric field, the strain induced in the ferroelectric phase couples with the magnetostriction. Hence due to the Villari effect the internal magnetization of the magnetic layer will change. Looking at the parameters involved in 2.22 , the direction of the effective magnetoelastic field will depend on the characteristics of the magnetic material, with regard to the coupling coefficients and the normalized magnetization, and the strain generated by the piezoelectric material below. The strain will be tensile or compressive depending on how the piezoelectric material responds to the applied electric field. Therefore, study of the materials involved and research to optimize the transfer of strain to the magnetic layer are important in order to make efficient devices with good coupling between the applied voltage and the produced magnetic field.

The magnetoelectric coupling coefficient can be described mathematically in two ways [22]:

$$\alpha_{ij}^{E} = \left(\frac{\partial B_i}{\partial E_j}\right) \tag{2.29}$$

when the change in magnetic induction B is due to the application of an electric field E or:

$$\alpha_{ij}^{H} = \left(\frac{\partial P_i}{\partial H_j}\right) \tag{2.30}$$

when the change in electric polarization P is due to the application of a magnetic field H [22]. This coupling is a tensor and in both cases it must give the same

result:

$$\alpha_{ij}^{E} = \left(\frac{\partial B_i}{\partial E_j}\right) = \left(\frac{\partial P_i}{\partial H_j}\right) = \alpha_{ij}^{H} \tag{2.31}$$

Knowing that:

$$P = \epsilon_0 \chi_e E \qquad B = \mu_0 \chi_h H \tag{2.32}$$

where ϵ_0 is the vacuum electric permittivity, χ_e is the electric susceptibility, μ_0 is the vacuum magnetic permittivity and χ_h is the magnetic susceptibility. 2.31 becomes:

$$\alpha_{ij} = \epsilon_0 \chi_e \mu_0 \chi_h \left(\frac{\partial E_i}{\partial B_j}\right) \tag{2.33}$$

Inserting 2.29 in 2.33 the final expression of the coupling is:

$$\alpha_{ij}^2 = \epsilon_0 \chi_e \mu_0 \chi_h \rightarrow \alpha_{ij} = \sqrt{\epsilon_0 \chi_e \mu_0 \chi_h} \tag{2.34}$$

There are various studies and various techniques to evaluate it in different composites but it remains quite complex considering that there are also quite other parameters to be taken into account concerning both thermodynamic, mechanical and magnetic aspects. In this sense, using AMR effect leads to evaluate the desired coupling in an indirect way without the need to know all these material parameters.

Chapter 3

Methodology

3.1 AMR devices

AMR devices exploit the anisotropic magnetoresistance effect, where the electrical resistance of a ferromagnetic material changes based on the angle between the electric current and the material's magnetization direction. The ability to characterize the magnetoelectric effect in a composite is the primary motivation behind the construction of these devices. Furthermore, understanding the physics behind the coupling is made possible by evaluating it using several devices with various geometries and fabrication methods. In fact, design is central to figuring out the best way to apply a strain and transfer it to the magnetic layer.

The devices studied in this thesis are like the one shown in Figure 3.1

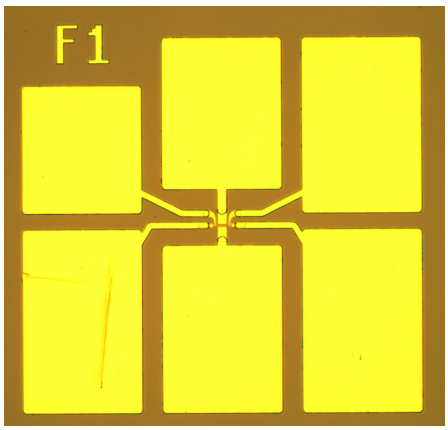

Figure 3.1: Image made by using an optical microscope of a studied AMR device.

They are planar structures in which a magnetic nanostrip lies on a ferroelectric material substrate. Recent studies conducted in my host group have shown that the best way to maximize the strain along the magnetostrictive strip is to arrange electrodes on either side of the strip and apply the same voltage. In this configuration the nanostrip is grounded. To read the resistance, it is necessary to apply

a current and measure the voltage of the nanowire. For this reason, a further four contacts shown in Figure 3.2 are required for measurement.

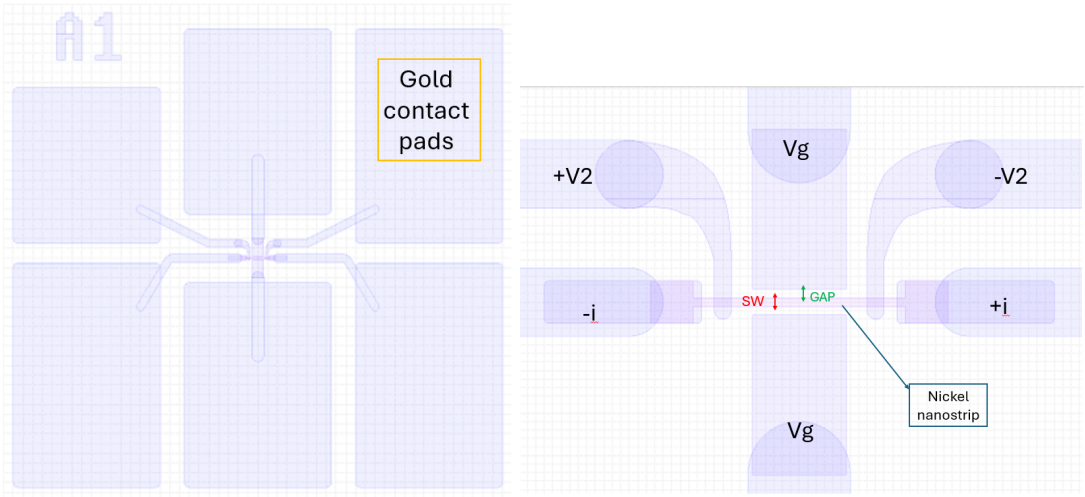

(a) **(b)**

Figure 3.2: Mask layout showing a sample device (a) and the respective voltages referred to the pads (b). The geometric parameters most studied in this thesis are also highlighted.

The materials used in this research were selected based on their magnetic properties, compatibility with device fabrication processes, and their ability to achieve high magnetoelectric coupling coefficients.

3.2 AMR devices fabrication

The fabrication of AMR devices demands highly controlled and precise processes to achieve a structure as ideal as possible. Indeed the performance of these devices is critically dependent on the integrity and quality of their layers and interfaces. Imperfections such as surface roughness, impurities, or structural defects can significantly degrade the device's performance by introducing unwanted magnetic noise, increasing resistance, and reducing sensitivity. Therefore, in order to reduce these imperfections and transfer the acquired knowledge to future devices, it is necessary to maintain an ideal fabrication process. The fabrication of these devices can be divided into three main steps that include deposition of the piezoelectric layer, magnetic phase, and gold electrodes and contacts to apply and read voltages.

3.2.1 Piezoelectric layer

The piezoelectric layer is mainly composed of *Ba-substituted lead zirconate titanate (BPZT)* $(Ba_yPb_{1-y})(Zr_{1-x}Ti_x)O_3$ thin film. It is a ceramic perovskite material that exhibits excellent piezoelectric properties and high dielectric constant. The addition of barium is used because it has been shown to improve the electromechanical

performance, boosts the dielectric integrity, and decreases grain size [25]. The deposition process consists of *pulsed laser deposition* (PLD) for which imec has developed recipes in the past to control the deposition of the material. PLD is a physical vapor deposition technique used to create high quality perovskite oxide thin-films on a substrate. In this process, a high-power pulsed laser beam is focused at the material that is the target, as illustrated in Figure 3.3. The energy from the laser ablates the target material, creating a plasma plume that contains ions, atoms, and molecules. This plasma plume then expands and deposits a thin film of the target material onto a substrate placed opposite the target.

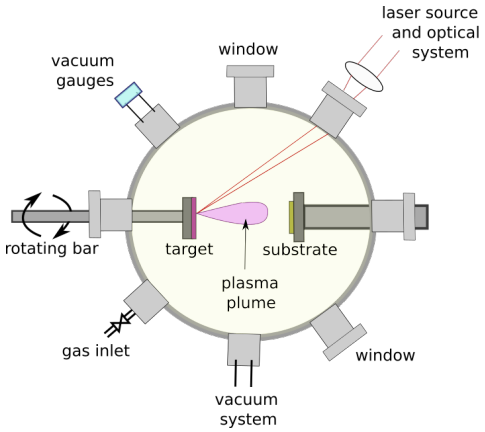

Figure 3.3: Pulsed Laser Deposition scheme: the laser absorbed by the target causes the plasma plume to form. When this reaches the substrate, a thin film will start to growth.

To get a good quality layer and to achieve the right stoichiometric ratio, it is important to use well defined values of temperature, energy, repetition rate, and oxygen pressure (since we are depositing oxides). In fact, an excess of oxygen would not get the target molecules to the substrate, while a defect in the latter would not allow a good stoichiometric ratio of the oxide. Similar discussions apply to temperature and repetition rate, the latter depending greatly on the nature of the target. In this case, 10 nm thick $LaNiO_3$ (LNO) has been deposited on a $750\mu m$ thick silicon substrate and 400nm thick *silica* SiO_2, obtained by thermal oxidation, using the following values:

Temperature	Energy	Repetition rate	Pressure $[O_2]$
500°C	540 mJ	33 Hz	0.1 mbar

Table 3.1: PLD parameters for LNO deposition

A thin LNO layer has been added to reduce the lattice mismatch between SiO_2 and $BPZT$ and to enhance the dielectric and piezoelectric properties of the latter [24].
Afterwards, 600 nm thick $(Ba_{0.1}Pb_{0.9})(Zr_{0.52}Ti_{0.48})O_3$ has been deposited on the LNO layer using the following values:

Temperature	Energy	Repetition rate	Pressure $[O_2]$
550°C	540 mJ	100 Hz	0.1 mbar

Table 3.2: PLD parameters for BPZT deposition

Next a step of chemical mechanical polishing (CMP) is needed since the resulting layer has a very rough surface. CMP has been performed using a silica-based slurry, but it's also important to define the rotation speed of the top and bottom plates and the down force that has to be applied to the sample. To get the best result low speed ($50rpm$ for both the top and the bottom plate) and low down force ($1.5psi$) have been used for 2 minutes. After a standard cleaning of the sample has been performed to remove all traces of particles or thin layers of oxide. In order to complete that, the samples were submerged for 10 minutes at 75°C in a SC-1 solution composed of five parts deionized water, one part ammonia water, and one part hydrogen peroxide. This was followed by a five-minute soak in isopropanol in an ultrasonic bath. [24].

3.2.2 Magnetostrictive layer

This layer corresponds to a magnetic nanostrip responsible for converting mechanical strain into magnetic energy. Very high magnetostriction coefficient magnetic thin films are necessary for efficient magnetization manipulation [26]. In addition having materials with low damping and narrow linewidth is good to reduce the microwave loss. Furthermore, growing magnetostrictive thin films on stiff substrates causes a clamping effect [27]. In literature there are many studies on different transition metal ferromagnets and their binary, like galfenol, or ternary alloy, like terfenol-D, whom magnetostrction coefficient can be very high. It is to be notice that they are not rare-earth elements so classical deposition processes can be used, making them suitable for many different applications. The integration of these materials with the state-of-the-art, however, has not yet been demonstrated. The usage of nickel in this situation successfully addresses these issues. Nickel has been extensively researched by my host team in imec. It has magnetic characteristics that have been verified, and has been shown to work with BPZT. Thus, using a known material such as nickel is significantly more favorable when comparing the effects of different deposition techniques, defects and geometries on the magnetoelectric coupling.

Initially, the substrate was cleaned by immersing it in acetone for 10 minutes. *Polymethyl methacrylate* (PMMA) was selected as the photoresist due to its suitability for electron beam lithography. PMMA is a polymer material that acts as a positive photoresist under certain conditions. This means that the polymer chains break into smaller chain during the irradiation process. So PMMA was heated to 165°C for 3 minutes to ensure proper adhesion and stability. Following this, the sample has been exposed to an electron beam using a pre-designed mask, transferring the desired pattern to the photoresist. Then it has been rinsed in a solution of

MIBK and IPA at 20°C for one minute.

Subsequently, metal deposition was performed using two different methods: sputtering and thermal evaporation, showed respectively in Figure 3.4a and 3.4b. Both methods involved depositing a thin seed layer of tantalum (Ta) with a thickness of 5 nm, followed by the deposition of a 20 nm layer of Ni. The primary difference between the two methods lies in the final step. In the sputtering process, an additional Ta capping layer can be deposited, which is not possible with the evaporation method. Consequently, the nickel layer deposited via evaporation is exposed to the atmosphere, leading to oxidation.

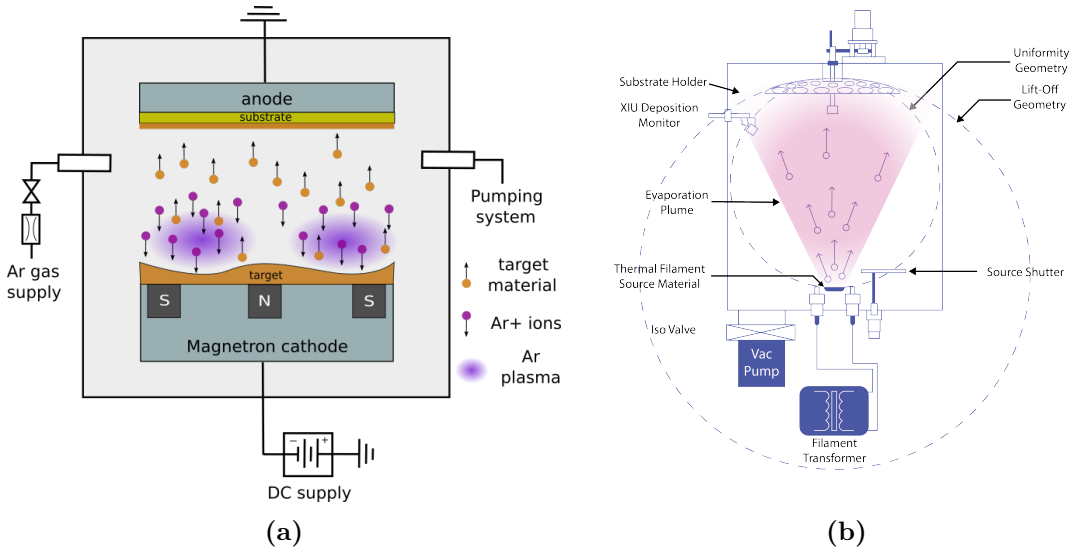

Figure 3.4: Scheme of DC sputtering (a) and thermal evaporation tools (b) used to deposit a thin film layer of nickel

This difference allowed for the examination of how the different deposition processes affect the device's behavior. Furthermore, the presence or absence of a capping layer can be useful to study its impact. For CoFeB devices only sputtering has been used.

Finally, a lift-off process in acetone was conducted to remove the photoresist, resulting in the finalized structure. A summary scheme of the process is shown in Figure 3.5.

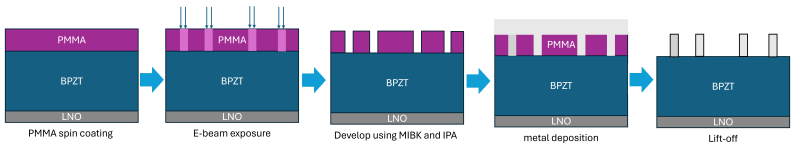

Figure 3.5: Deposition process made by transferring the pattern using e-beam litography and lift-off process

3.2.3 Gate electrodes and contacts

For gate electrodes, electron beam lithography was also used to transfer the previously designed mask pattern so this step has already been described in the previous section. It is to be noted that making the metal contacts is a more challenging procedure than actually fabricating the contact pads. Using an e-beam instead of optical lithography in the lab allowed for an excellent resolution and a better alignment. In the study of AMR, precise measurements are required for trying to minimize parasitic effects that might make the results unreliable. Therefore, the choice of metal for electrodes and contacts is very important. Gold has been chosen as metal contacts for several reasons. First, gold possesses high electrical conductivity. In addition, gold has low contact resistance, which means that the junctions between gold and other materials in the device offer minimal resistance. This is essential to reduce signal losses and improve measurement reliability. Low contact resistance also contributes to better device sensitivity, as changes in resistance due to the AMR effect can be detected more easily.

For all these reasons gold is the perfect choice dealing with low-voltage applications [21].

Gold was deposited using the same sputtering tool described before, and then a gentle lift-off process was used to remove the PMMA.

3.3 Experimental setup

Experimental data were taken by measuring devices in cleanroom using mainly a tool called *SOT Hall setup* shown in Figure 3.6.

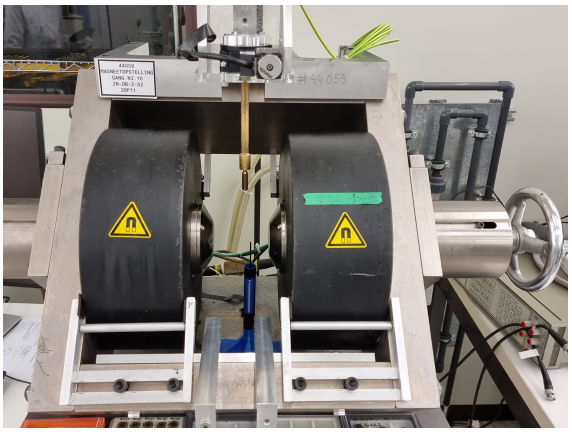

Figure 3.6: Picture of the SOT hall experimental setup used for AMR measurements. The two electromagnets, the sample holder connected to the motor and the hall magnetometer can be observed.

This tool consists of a dipole electromagnet that can generate magnetic fields of up to 2T depending on the spacing between poles. The sample holder is in the middle of the magnet and, in according to the type of attachment, it allows in plane

or out of plane measurements to be made. For the device characterized in this thesis the in-plane probe shown in Figure 3.7b has been used. The tool includes a current source and a voltage source. The DC voltage source was used to apply voltage to the gate electrodes, while the current source, in conjunction with a multimeter, was used to apply current to the device and measure the DC voltage for resistance calculation.

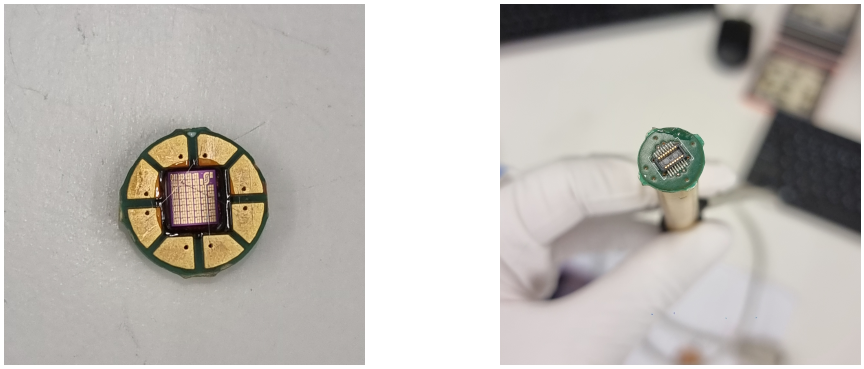

(a) **(b)**

Figure 3.7: Device bonded on a PCB (a) and in-plane probe (b) for the measurements at the SOT setup

Before characterization, the device must first be attached to a PCB. To do this, a drop of photoresist is deposited onto the PCB, placing the device on top, and heated to 100 degrees for 3 minutes. After making the wire bondings between the device and the PCB, it is attached to the in-plane probe and then placed on the rotating sample holder as figure3.8 shows.

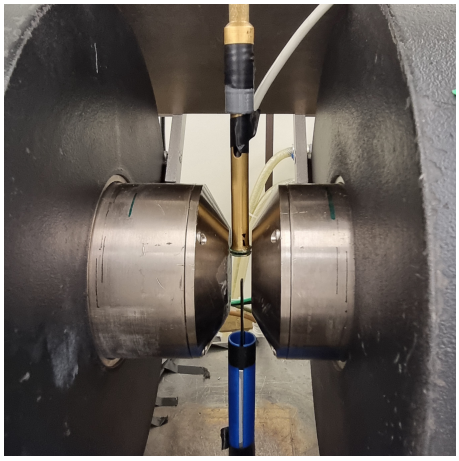

Figure 3.8: Setup during measurements. The Hall probe is used to measure and save the intensity of the applied magnetic field

The sample holder is connected with a small motor that allows the sample to be rotated therefore the angle between the magnetic field lines and the current can

be adjusted. The magnets, motor, and three Keithley instruments are controlled by a PC using a LabVIEW program shown in Figure 3.9. This program allows the execution of complex measurements by sweeping the field and angle within the designated voltage and angle range.

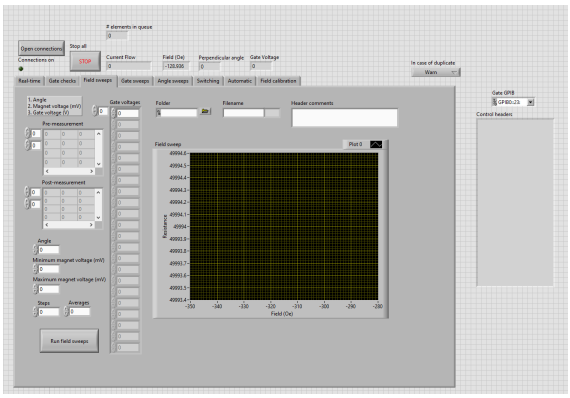

Figure 3.9: Screenshot of the LABview interface. This presents different cases depending on the type of measurement desired. Each case allows you to define the maximum and minimum values to make the parametric sweep relative to the measurement and to set those values that remain constant during the sweep.

3.4 Simulations

The simulation of AMR devices requires the use of advanced software to accurately analyze their behavior and properties. In this context, *COMSOL Multiphysics* and *Mumax* are essential tools for conducting precise and detailed simulations. *OOMMF* has been used for the visualization of the micromagnetic simulations. The integration of these tools allows for a deep understanding of the mechanical, electrical, and magnetic interactions within these multilayered magnetoelectric devices.

3.4.1 COMSOL Muliphysics

COMSOL Multiphysics is a simulation software used in many different physics and engineering applications, especially coupled phenomena and multiphysics [30]. The examination of the stress resulting from applied voltage has been made, including its distribution along the strip and the influence of various parameters on the overall system. Initially, the device has been designed using software, where all essential parameters for electrostriction calculations were specified and shown in Figure 3.10.

Name	Expression	Value	Description
t	0[s]	0 s	Time parameter
PZT_heigl	0.4 [um]	4E-7 m	PZT height
L	20e-6[m]	2E-5 m	Magnet length
W	1e-6[m]	1E-6 m	Magnet width
H	20e-9[m]	2E-8 m	Magnet height
alpha	4.2e6[m/F]	4.2E6 m/F	Inter-domain coupling
a	6.4e5[V/m]	6.4E5 V/m	Domain wall density
c	0.2	0.2	Polarization reversibil
k	1e6[V/m]	1E6 V/m	Pinning loss
Ps	0.425[C/m^2]	0.425 C/m²	Saturation Polarizatio
Q11	3.579e-2 [m^4/C^2]	0.03579 m⁴/(	Electrostriction couplii
Q12	-5.335e-3 [m^4/C^2]	-0.005335 m	Electrostriction couplii
Q44	1.923e-2 [m^4/C^2]	0.01923 m⁴/(	Electrostriction couplii

Figure 3.10: Parameters used in COMSOL

Subsequently, the geometry was defined by modeling the PZT substrate, the nickel nanostrip, and the gold contacts. The final structure obtained is shown in Figure 3.11.

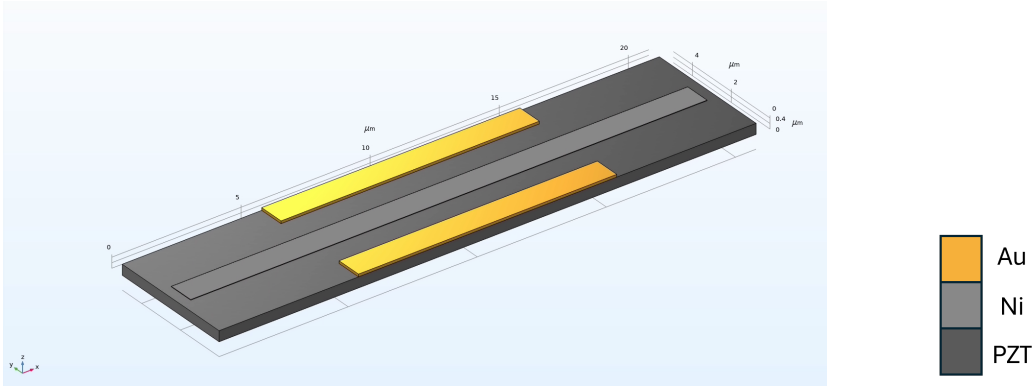

Figure 3.11: AMR device in COMSOL, nanostrip width=1μm, length=20μm, thickness=20nm

Each block of the geometry represents a domain of the system. This distinction is crucial for accurately associating physical models to define boundary conditions and contacts. For the mechanical models, the entire structure was included since every part of the device is subject to strain. For the electrical model, initial conditions were established: the ground state was set at the bottom of the nickel strip, and the electrical potentials were defined for the gold electrodes. The *electrostriction* model was specifically assigned to the PZT to calculate the induced stress. Lastly, to enable simulation, a fine mesh was required. Running the simulation with an applied voltage of V = -3V, as an example, yielded the following 2D images:

As observed in Figure 3.12, this configuration produces uniform stress at the center of the nanostrip. The strain tensor components that significantly impact the device are ϵ_{yy} and ϵ_{zz}, while the other components are negligible. The stress is 2×10^{-4} along the z-direction and doubles the intensity with opposite sign, thus -4×10^{-4}, in the y-direction. This suggests that the impact of the y-component will be predominant therefore, it can be assumed that the magnetic field yielded by the magnetoelectric effect is primarily transverse. By applying the same procedure,

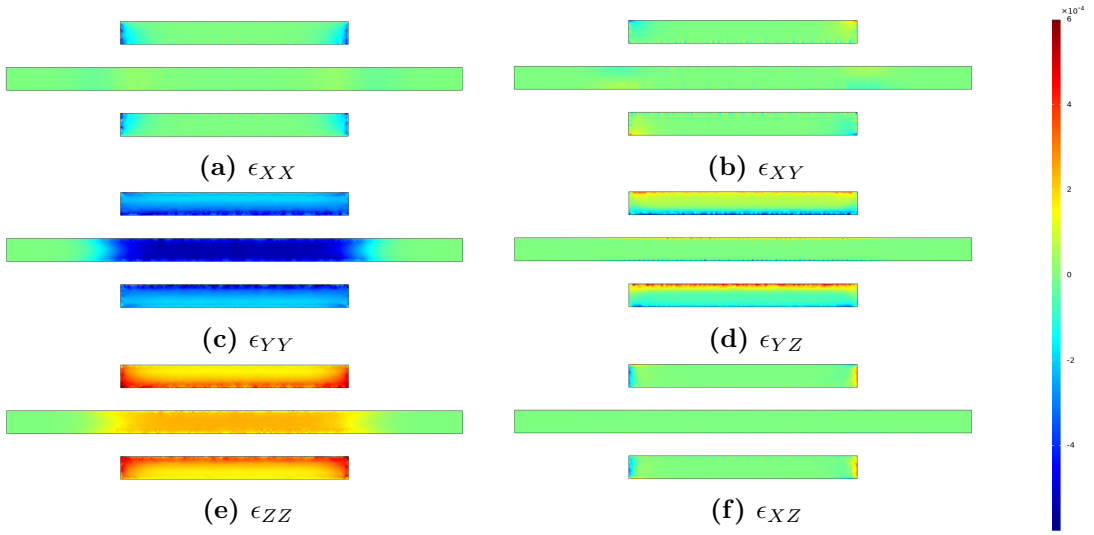

Figure 3.12: 2D maps of the strain tensor components obtained by applying V=-3V. To be noted that the only non-zero components are $\epsilon_{zz} = 2 \times 10^{-4}$ and $\epsilon_{yy} = -4 \times 10^{-4}$.

the same configurations with different widths have been simulated by varying the strip width. The values of the relevant components for each configuration, obtained when the devices were brought to the saturation point, are shown in Figure 3.13.

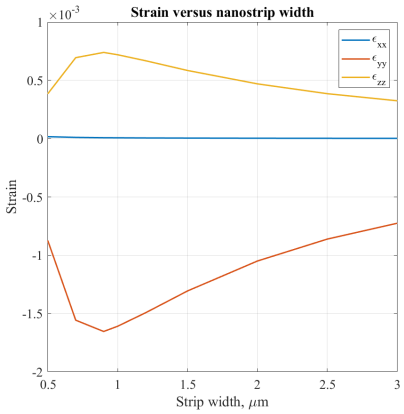

Figure 3.13: Graph of the saturation's normal components of strain as width varies. When the width is somewhat less than $1\mu m$, a larger strain in absolute value is seen, but ϵ_{xx} always remains negligible.

An increase in strain is predominantly noted for widths smaller than one, followed by a decrease for widths greater than one. This behavior is expected because a larger width leads to more distributed stress, reducing localized strain. It's also important to remember that changing the strip's thickness changes the distance between the electrodes and the strip. Because of the greater gap that a narrower strip creates, $0.5\mu m$ thick strips cause less stress than thicker ones.

To understand whether the width favors one strain component over another, it is possible to examine if ϵ_{yy} and ϵ_{zz} increase or decrease in the same way.

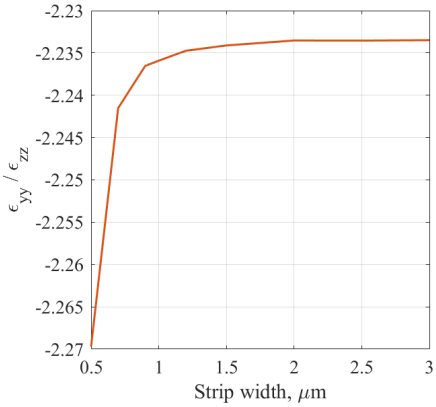

Figure 3.14: $\epsilon_{yy}/\epsilon_{zz}$ for different widths

From the figure 3.14, it is evident that when the strip is less than 1 µm thick, the y-component plays a slightly larger role, probably due to increased lateral confinement effects. For larger widths, the ratio remains more or less constant. This indicates that when the width exceeds one micrometer, the applied tension has similar effects on both the z and y components.

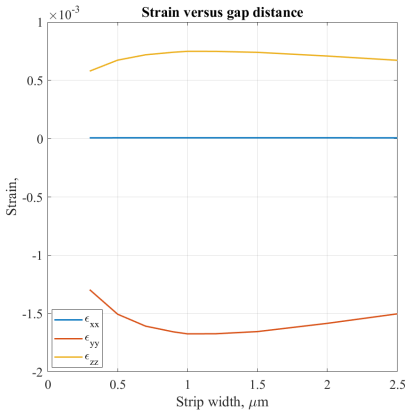

Figure 3.15: Graph of the saturation's normal components of strain as the gap between the electrodes and the nanostrip changes. The strain in the strip is less than at greater distances if this gap is too small. With a gap of $1\mu m$, the strain is maximum.

A similar trend to the previous one can be seen in Figure 3.15 when varying the electrode-to-strip distance. However, the strain component values do not vary as drastically as in the other case. However, it is observed that ϵ_{yy} decreases faster than ϵ_{zz} in absolute terms as the distance increases. This suggests that, with a larger gap, a significant portion of the energy from the applied electric field dissipates more transversely. Some of these values will serve as important inputs for deriving the coupling coefficient from the experimental data.

3.4.2 Mumax3

$Mumax^3$ is a powerful NVIDIA CUDA21 based, graphics-processing-unit (GPU) accelerated, micromagnetic software package [29]. Like all the other micromagnetic simulation tools, it allows for the modeling of magnetization dynamics by solving the LLG equation described in2.27. To do this, the simulator discretizes the magnetic structure into small elements with a size and a number defined at the beginning of the simulation code. Each element has its own magnetization that is normalized to the saturation magnetization ($m(r,t) = M(r,t)/M_S$) and will be subjected to a certain magnetic field. This magnetic field corresponds with the effective magnetic field defined in 2.23 thus will be the sum of all the different interactions. Using phenomenological parameters, the user defines all energy terms (or derived effective fields) [29]. Then in the code, after defining the geometry of the structure, we define the parameters that will be used to calculate the associated magnetic field. The choice of parameters depends on the system and the phenomenon to be studied. In the study of this thesis, the parameters defined were the saturation magnetization, the exchange stiffness, the first and second magneto-elastic coupling constant.The damping term had no effect on the final outcome because the work in this thesis was carried out in direct current. It is therefore acceptable to manipulate the damping term in order to speed up the simulation time while remaining confident of obtaining trustworthy results. The parameters used for the nickel and CoFeB simulations are summarised in the table 3.3:

	Ni	CoFeB
M_s	$4 \times 10^5\ A/m$	$13.6 \times 10^5\ A/m$
A_{ex}	$10^{-12}\ J/m$	$18 \times 10^{-12}\ J/m$
B_1	$7.85 \times 10^6\ J/m^3$	$-6.9 \times 10^{12}\ J/m^3$
B_2	$7.85 \times 10^6\ J/m^3$	$7.1 \times 10^{12}\ J/m^3$

Table 3.3: Parameters used in micromagnetic simulations for Ni and CoFeB

These parameters were taken from my host team's database at *imec*. In particular the saturation magnetization was taken by using the *vibrating sample magnetometry* (VSM) analysis.

3.4.3 Simulation results

Initially, the focus was on applying a longitudinal and a transverse magnetic field to the nanostrip to observe its response. The width of the nanostrip has been varied to examine how changes in this dimension affected the coercivity and the hysteresis loop. These differences provided information about the size-dependent magnetic properties and aided in figuring out the ideal proportions for the desired magnetic qualities.

Coercivity is inversely correlated with nanowire width, according to simulations, and becomes increasingly noticeable as width declines. With wider widths, this

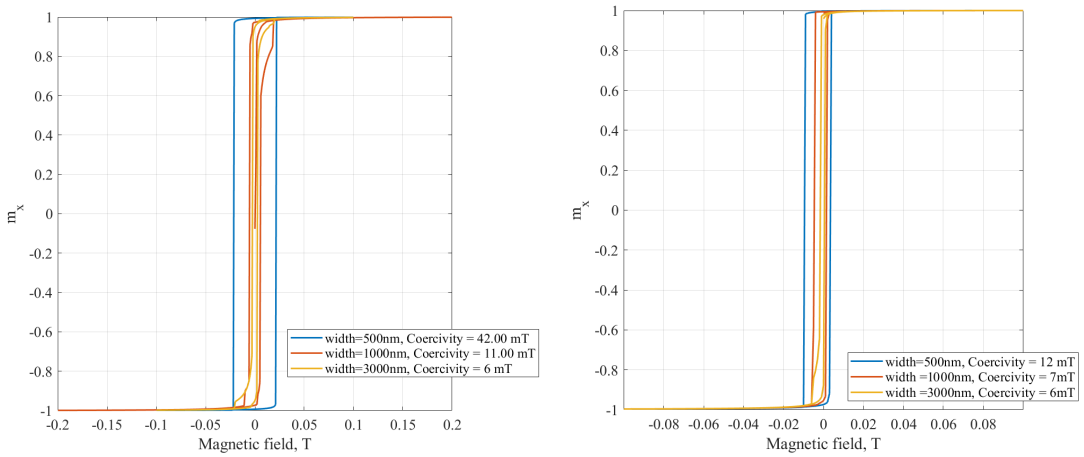

(a) *CoFeB* **(b)** Ni

Figure 3.16: CoFeB and Nickel hysteresis loop produced by applying a changing longitudinal magnetic field along the x direction

effect becomes much less pronounced. For example, there is very little coercivity variation between widths of 1000 nm and 3000 nm in the case of Nickel as it is possible to observe in Figure 3.16. This illustrates how the material gets harder as the strip gets thinner because shape anisotropy has a bigger effect. Furthermore, a softer material will respond to external magnetic disturbances more responsively.

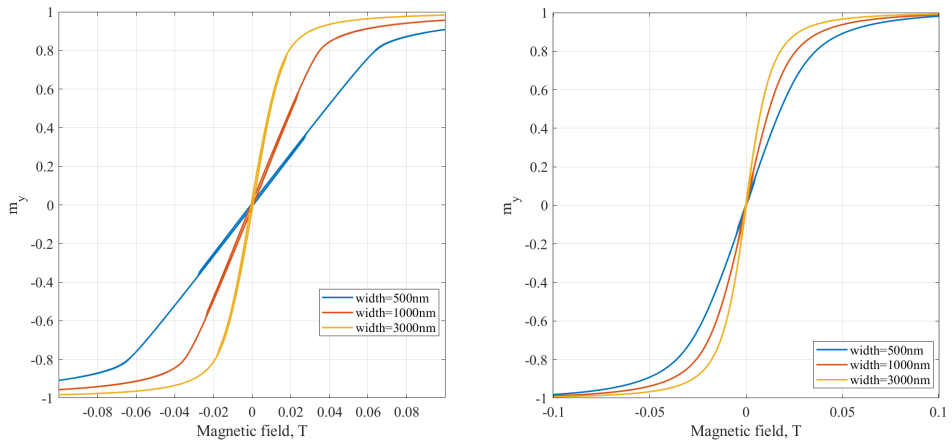

(a) *CoFeB* **(b)** Ni

Figure 3.17: CoFeB and Nickel hysteresis loop produced by applying a changing transversal magnetic field along the y direction

The transverse magnetic field hysteresis in Figure 3.17 provides important insights. For example, nickel behaves as though it has no transverse coercivity, but CoFeB exhibits a small one. The slope of these hysteresis curves also indicates the anisotropy of the material. Remarkably, in higher fields with very small widths, a

realignment occurs. There is no doubt that the hardness of the material impacts the steepness of this slope. On the other hand, the x component shown in Figure 3.18 exhibits the exact opposite behavior.

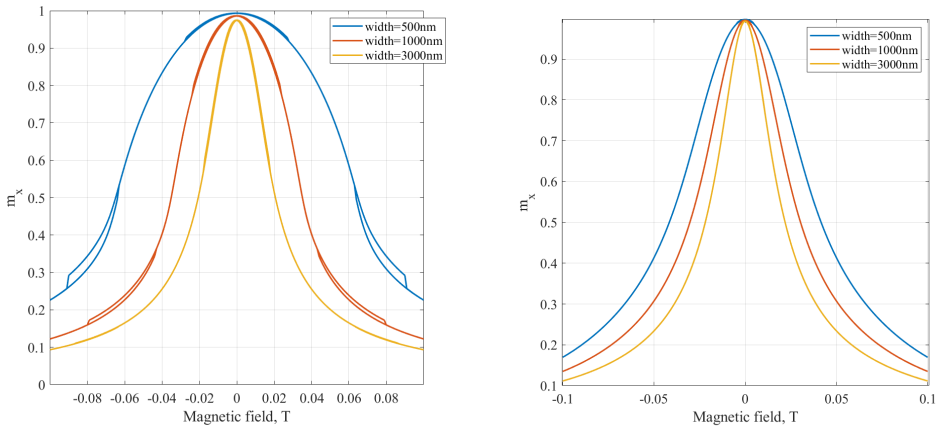

(a) $CoFeB$ **(b)** Ni

Figure 3.18: CoFeB and Nickel hysteresis loop produced by applying a changing transversal magnetic field along the y direction

With the width set to $1\mu m$, a detailed analysis was performed to understand the domain behavior within the nanostrip. By running a simulation varying only strain, it is observed in Figure 3.19 that the angle of magnetization decreases rather slowly for high negative strain values. It then quickly decreases as soon as the strain becomes positive. This means that the positive strain on the strip favours longitudinal magnetization. This was expected since positive strains are tensile, which causes the strip to stretch and squash by increasing form anisotropy and promoting magnetization along the easy axis.

Using OOMMF it is possible to plot some 2D maps showing in detail how the strain modifies the domain. At the initial state in Fifure3.20, the strip shows predominantly longitudinal magnetization as expected due to its shape. Note in detail the domains present along the edges. This is mainly due to the fact that anisotropy plays a greater role at the edges.

Analyzing figure 3.21, one immediately notices that the structure exhibits numerous domains due to strain. Reducing the strain to -1.5×10^{-4} reveals how the domains begin to align longitudinally. Additionally, the the various domains appear slightly shifted, indicating that the magnetic field caused by the strain is able to influence their movement. As expected for a positive strain almost all the domain are aligned along the longitudinal axis.

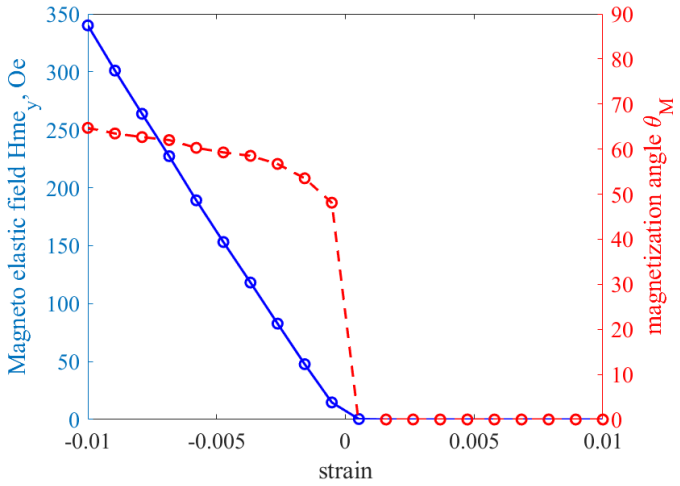

Figure 3.19: Hme_y and magnetization angle versus strain for a Nickel nanostrip with a width of $1\mu m$

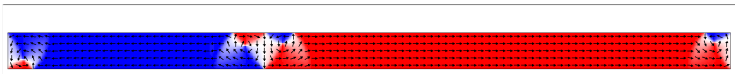

Figure 3.20: Initial state. The nanostrip has a length of $20\mu m$, width of $1\mu m$, thickness of 20nm. Note the presence of edge domains due to anisotropy

(a) $\epsilon_{yy} = -3 \times 10^{-4}$

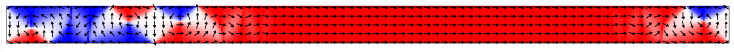

(b) $\epsilon_{yy} = -1.5 \times 10^{-4}$

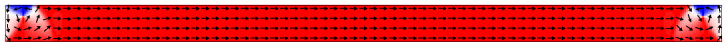

(c) $\epsilon_{yy} = 0.5 \times 10^{-4}$

Figure 3.21: magnetization patterns visualised via OOMMF. In the first pattern (a) the magnetoelastic field has such an intensity that it creates magnetic domains along the nanostrip. In (b), it can be seen that by reducing the intensity, it is unable to hold the domains as before. Applying positive strain (c), magnetization is favoured along the longitudinal direction

The fundamental mechanisms have been determined by studying the migration of magnetic domains. It was demonstrated that when subjected to strain, domain

walls nucleate and propagate, causing magnetic domains to reorient. Understanding the switching mechanisms and the stability of the nanostrip's magnetic state is dependent on domain motion. However, these results refer to ideal structures. In reality, other elements, like as defects and grain boundaries, have an equal impact on the actual magnetic field, which is not merely magnetoelastic.

3.5 Measurement

A significant number of devices were measured, but the only devices that provided meaningful data are shown in 3.4. All of these devices have a *20 nm* thick magnetostrictive layer in nickel. To distinguish the various samples, H21 and H22 are the names given to the devices obtained using sputtering and thermal evaporation, respectively. As mentioned in Section 3.2.2 , one of the main differences between the two coupons is the presence of a capping layer in the sputtered devices. Hence, the nickel in the H21 coupon devices is not in direct contact with the atmosphere, preventing oxidation. In contrast, nickel in the H22 samples do not possess a specific capping layer. As a result, the surface will have a thin layer of nickel oxide.

Coupon	Device name	Gate Length	Strip width	Gap
Sputtered nickel	H21 AMR STATS B1	11000 nm	1000 nm	1000 nm
	H21 AMR GAP D1	11000 nm	1000 nm	500 nm
	H21 AMR SW B2	11000 nm	500 nm	1000 nm
Evaporated nickel	H22 AMR STATS B1	11000 nm	1000 nm	1000 nm
	H22 AMR GAP H1	11000 nm	1000 nm	1300 nm
	H22 AMR SW H1	11000 nm	3000 nm	1000 nm

Table 3.4: AMR devices studied in this thesis. Each of them has the same length and thickness. The geometric parameters that change are the strip width and the gap between the nanostrip and the electrodes.

Utilizing parametric sweeps of the voltage, applied magnetic, and angle between the device and the magnetic field lines, measurements were made to determine whether the devices show signs of the magnetoelectric effect.

3.5.1 Angle sweep

Angular sweep refers to measurements made by rotating the sample in the middle of a strong magnetic field and keeping a constant or null voltage. Doing this it is possible to see the *sine* dependency of the resistance and in principle how different voltages affect the curve. Also, this first step is critical to figure out what angle to go to in the LabView program to precisely position the sample transversely or longitudinally for subsequent measurements. Recalling that AMR effect is described by 2.28, it is possible to plot the variation of the magnetization angle with respect to the angle of the motor. As it's possible to see from the pictures, all the devices show AMR effect.

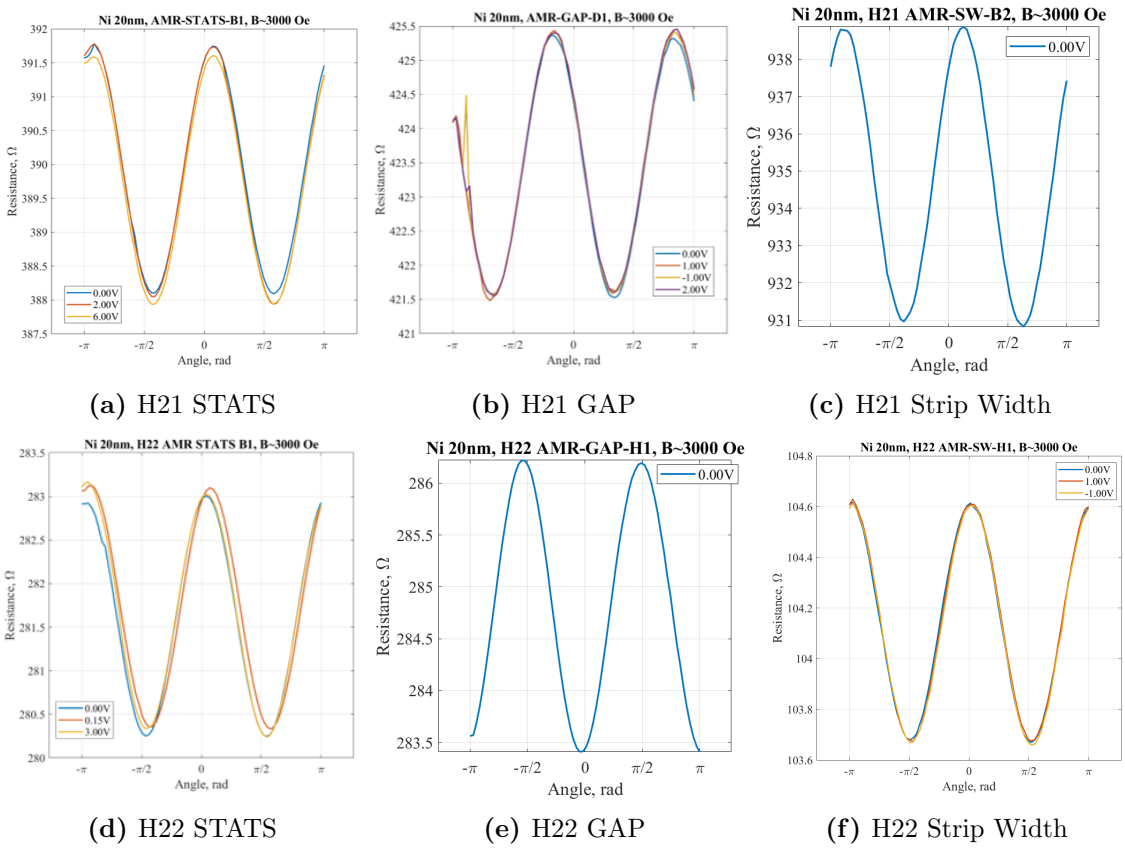

(a) H21 STATS **(b)** H21 GAP **(c)** H21 Strip Width

(d) H22 STATS **(e)** H22 GAP **(f)** H22 Strip Width

Figure 3.22: Angle Sweep measurements

In any case important considerations about the state of the devices can be made by comparing the values of the resistors. Considering pictures 3.22a and 3.22b, for both the geometry is the same and they were built in the same coupon. Their resistances, however, are very different from each other. This indicates that although the geometry and fabrication method is the same, the small imperfections in the structure turn out to have non-negligible effects dealing with thin films. Then, as easily imagined but still important to check to estimate the correct fabrication of the magnet, halving the width of the strip the resistance doubles, as is shown in Figure 3.22c, instead in 3.22f increasing the width threefold results in the resistance decreasing by a factor of three. Similar observations could be made for the devices in coupon H22 but remember that these, not having a capping layer, have an oxidized layer of a thickness unknown to us.

3.5.2 Field sweep

In a field sweep measurement, the sample is exposed to a changing magnetic field at a fixed angle. In according to the angle two different hysteresis loops can be seen. Applying an electric field, the magnetoelectric effect occurs affecting the shape of the loop as will be discussed later. If the angle between magnetic field lines and the nanostrip is 90 degrees, the transverse hysteresis loop will be obtained, otherwise

the longitudinal one. The angle will be set according to the values obtained during the angle sweep. However, SOT setup is not the optimal choice for initial screening and quick comparison of coercivity on various devices. This is because bonding must be done to measure in that setup, but considering that devices with different thicknesses are in the same coupon, it is not possible to bond multiple devices from the same coupon in the same PCB. Therefore, for a quick study, it was decided to make the measurements using a different magnetic probe station in another laboratory that allows measuring various just by using some needles.

3.5.3 Gate Sweep

In gate sweep measurements, specific angles and magnetic fields are fixed while only the applied voltage varies. These measurements are very useful for observing the effects of different voltages and to evaluate the magnetoelectric coupling. Moreover, to thoroughly investigate these effects, measurements have been conducted both without any applied magnetic field and with magnetic fields of increasing intensity.

Chapter 4

Results and discussion

4.1 Angle sweep results

The data obtained by doing an angle sweep are not used to calculate the magneto-electric coupling because the application of a strong magnetic field (of about 3000 Oe) compromises any attempt at calculation. However, from 2.28, it is possible to derive the relationship linking the resistance values to the magnetisation angle.

$$\theta_M = \cos^{-1}\left(\sqrt{\frac{R - R_\perp}{R_\parallel - R_\perp}}\right) \tag{4.1}$$

In this way, it can be observed in Figure 4.1 that each maximum in the graphs corresponds to a magnetisation angle of pi/2 as expected. For every minimum, the angle is 0. This is true for every device, as it is due in itself to the physics behind the AMR effect.

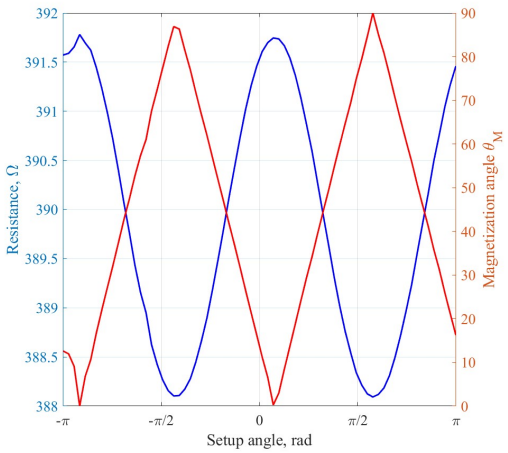

Figure 4.1: Relationship between the angle sweep done previously and the angle of magnetisation.

4.2 Field sweep results

The first data collected using needles instead of bonding produced the following graphs shown in Figure 4.2.

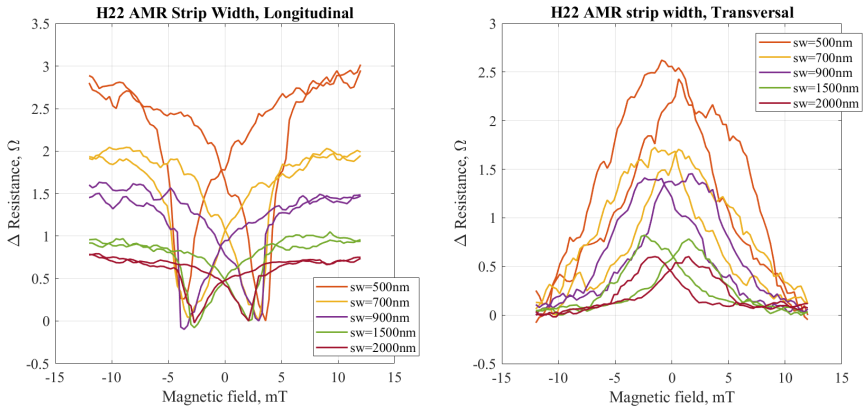

Figure 4.2: Field Sweep measurements for different strip widths

The graphs obtained illustrate how resistance varies as a function of magnetic field strength. It's important to consider the influence of geometry on the direction of magnetization when analyzing these changes. The variations in transverse and longitudinal resistance are markedly different due to their origins in distinct physical phenomena:

- Longitudinal hysteresis loop shows that the change in longitudinal resistance is primarily driven by domain wall motion. In this context, the switching field is typically associated with the domain wall nucleation field. This field is generally independent of the strip width, meaning that changes in the width of the strip do not significantly affect the switching field in the longitudinal direction. Conversely, the change in transverse resistance is driven by the magnetization precess itself. In narrower strips, a broader peak is observed in the resistance curve. This broadening is attributed to shape anisotropy, which causes the narrower strip to resist switching under a transverse magnetic field more than a wider strip. The shape anisotropy introduces additional complexity to the switching behavior, as the narrower geometry enhances the stability of the magnetization, making it less susceptible to changes induced by the transverse magnetic field. The longitudinal switch provides valuable insights into the coercivity of the magnetostrictive layer. Specifically, the distance between the two peaks in the resistance graph corresponds to the coercive field of the hysteresis loop. The fundamental principles of magnetic behavior can be understood by considering that all magnetic domains align with a strong magnetic field. In this aligned state, the resistance of the device is at its maximum due to the increased probability of scattering processes.

As the magnetic field strength decreases, domain walls begin to emerge. The formation of these domain walls reduces the overall alignment of the magnetic domains with the applied field, causing a decrease in resistance. Consequently, the resistance value will not reach the absolute minimum observed during angle sweeps. This is because the magnetisation history and resulting anisotropy maintain a certain level of misalignment among the magnetic domains, preventing the complete minimization of resistance;

- Transverse hysteresis loop instead confirm that for transverse measurements the magnetic domains are oriented perpendicular with respect to the direction of the current. As a result, electrons traveling through the nanostrip encounter fewer scattering events, leading to a minimal resistance. However, as the intensity of the magnetic field decreases, the domains quickly redistribute themselves according to the anisotropy of the strip. This realignment significantly increases the resistance value.

By conducting measurements on the SOT setup, more reliable results have been obtained in terms of coercivity and resistance readings. Additionally, the capability to apply voltage allowed us to study its effects on the devices. Considering initially the first device in Table 3.4. The results of its field sweep are shown in Figure 4.3.

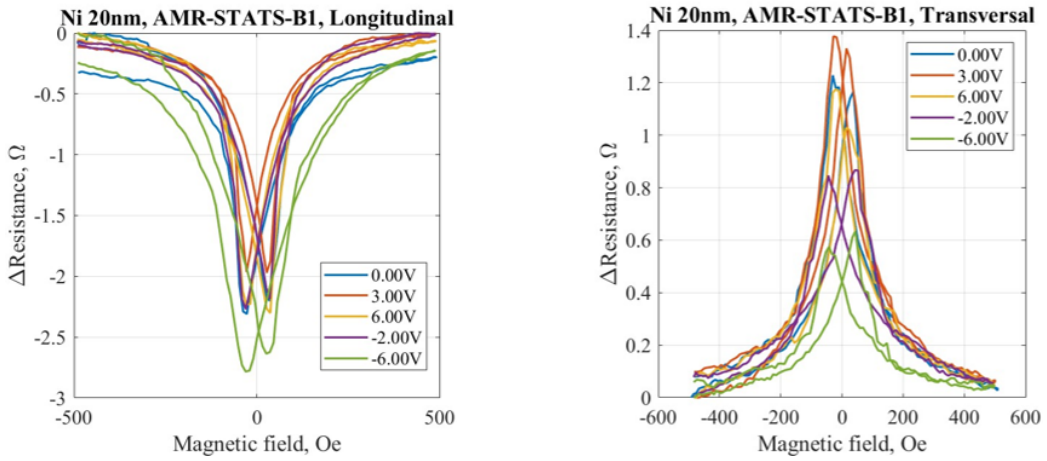

(a) **(b)**

Figure 4.3: Longitudinal (a) and transverse (b) field sweeps for sputtered nickel with strip width equal to 1000nm and gap of 1000nm

Regarding the longitudinal measurements, as expected, the coercivity remains constant regardless of the applied voltage, meaning the minimum resistance values occur at the same magnetic field strengths. Depending on the applied voltage, the curves become either smaller and more compressed or narrower and deeper. This variation is attributed to the magnetoelectric effect, which generates that magnetoelastic force that influence the effective magnetic field experienced by the strip.

With regard to transversal measurement shown in similar considerations can be made. In this case, though, the magnetoelastic field is in some cases strong enough to hold the magnetization directed perpendicularly even in the presence of small magnetic fields. To get a clearer picture of this, it is possible to represent how the magnetization angle varies as a function of the magnetic field for a specific applied voltage. From the angle sweep measurements, the values of $R_{\perp}$ and $R_{\parallel}$ are known. This makes it possible to compare the variations in the angle for various voltages in both longitudinal and transverse measurements in Figure 4.4.

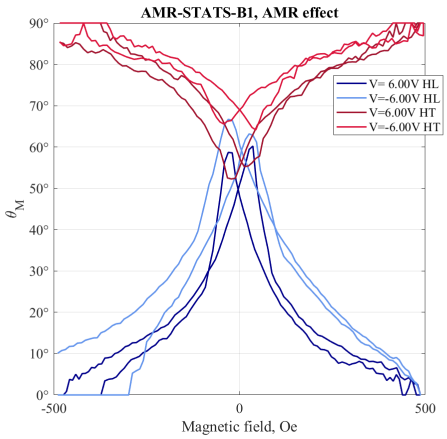

Figure 4.4: Magnetization angle versus magnetic field

Halving the distance between the electrodes and the nanostrip reduce the effect of the strain, as seen from simulations. This is proven by the fact that for different voltages the obtained curves in Figure 4.5 appear very similar to each other, especially for longitudinal ones. Moreover, having such a narrow gap leads to a limitation on the maximum voltage that can be applied.

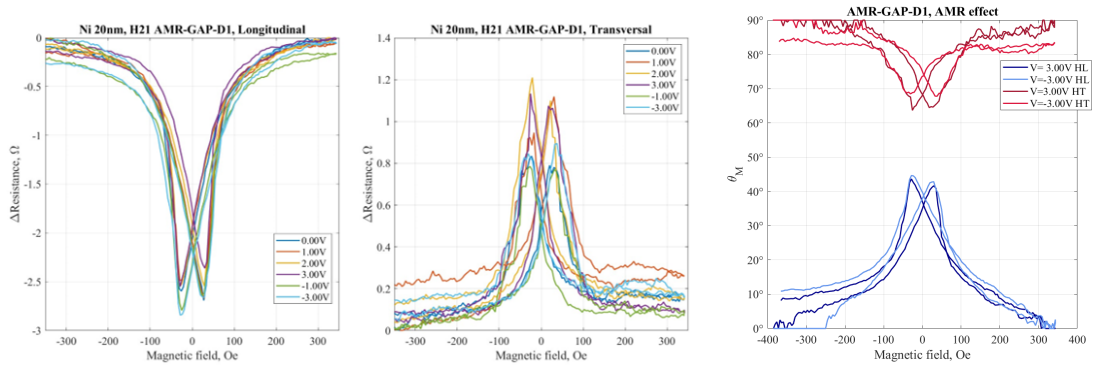

(a) **(b)** **(c)**

Figure 4.5: Longitudinal (a) and transverse (b) field sweeps for sputtered nickel with strip width equal to 1000nm and gap of 500nm. (c) shows how the magnetization varies with the field.

By reducing the width of the nanostrip with respect the first discussed device, the first thing immediately observable in Figure 4.6 is the larger AMR effect due to the fact that the strip is thinner.

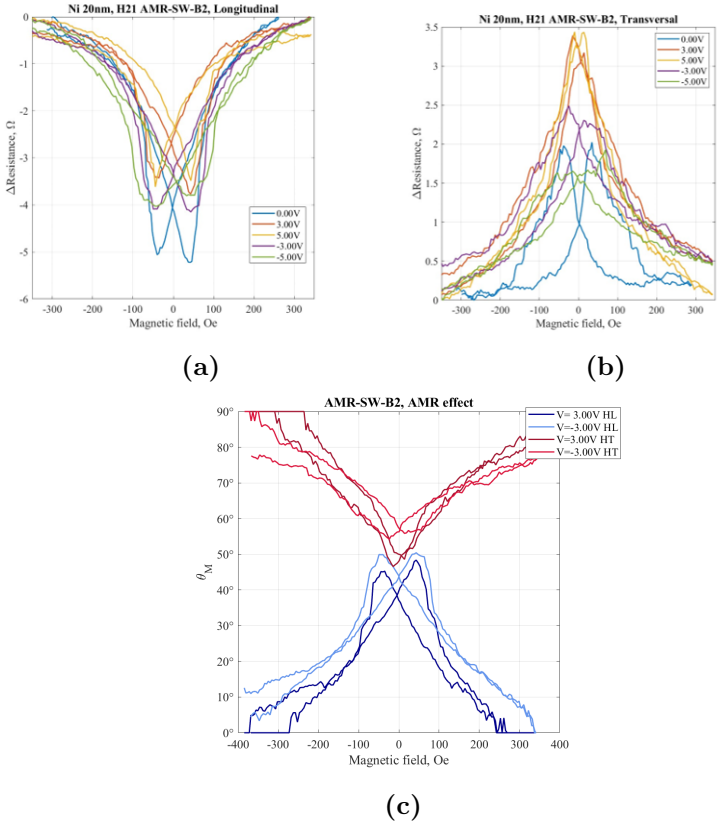

Figure 4.6: Longitudinal (a) and transverse (b) field sweeps for sputtered nickel with strip width equal to 500nm and gap of 1000nm. (c) shows how the magnetization angle varies with the field.

In any applied field, the magnetoelectric effect is easily observable. The applied voltage seems to better align the magnetic domains transversally during the transverse sweep, indicating a strong coupling effect that improves domain alignment in this direction.

Turning now to the analysis of devices with evaporated nickel, it is possible to investigate possible differences due to the material being softer. Furthermore, the absence of a capping layer can lead to conclusions regarding the influences of this oxide on the surface. The measured field sweeps for these devices are shown in Figure 4.7.

The most immediately noticeable observation is that the difference between the maximum and the minimum resistance is lower compared to the previous cases. This reduction is probably due to the oxidation of nickel, which leads to the creation of surface defects. These defects have several significant impacts, as they disrupt the uniformity of the magnetic domains and so degrade the magnetic properties of the material [14]. Despite this, the strip responds to the same voltages as in the

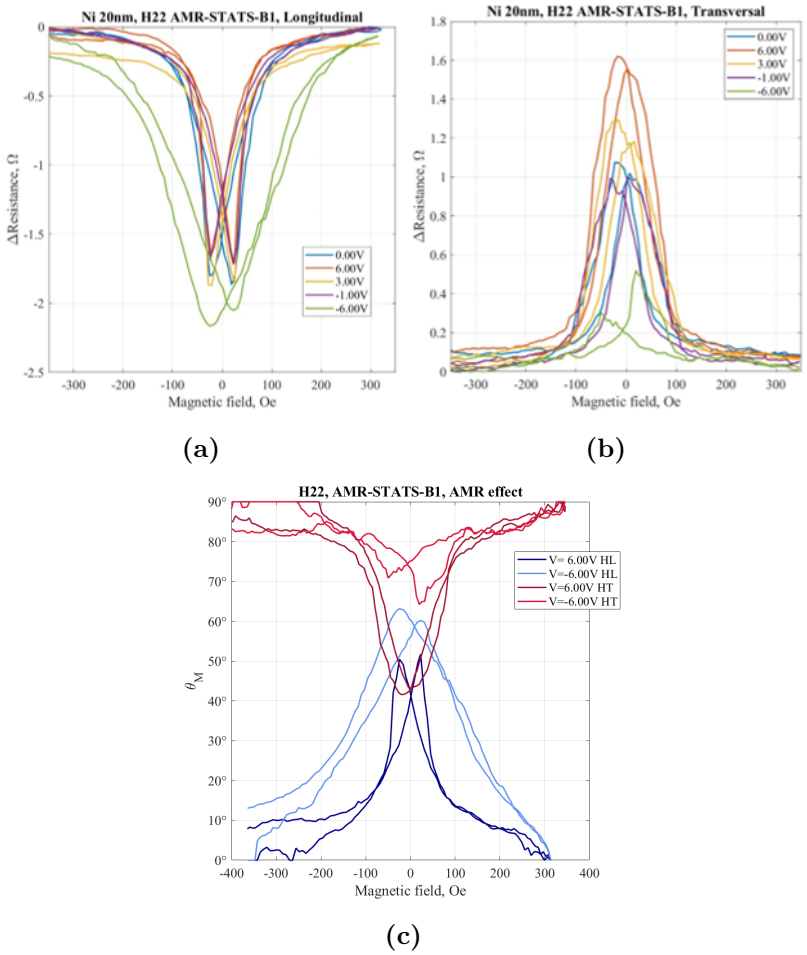

Figure 4.7: Longitudinal (a) and transverse (b) field sweeps for evaporated nickel with strip width equal to 1000nm and gap of 1000nm. (c) shows how the magnetization angle varies with the field.

previous case, but the magnetoelectric effect is considerably stronger. In fact, in the longitudinal measurement, for V=6V the magnetization angle reaches almost 40° (as shown in 4.7c), rather than 50° like in the other. This is due to various factors dependent on the nickel deposition process. With evaporated nickel, the residual stress is lower and the BPZT will be less damaged. All this will increase the coupling. Since other devices without the capping layer have been considered, the latter graphs will be taken as a reference. This will still allow us to consistently understand the effect of electrode spacing and strip thickness.

Wanting to compare how coercivity also varies, the longitudinal field sweeps were compared showing that the coercivity value obtained experimentally for H21 STATS coincide with the value obtained from simulations as shown in Figure 4.8.

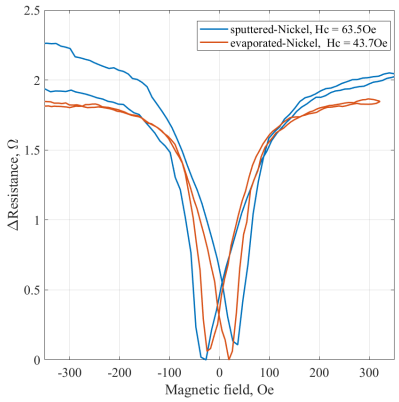

Figure 4.8: Comparison between the longitudinal hysteresis loop for sputtered-nickel vs evaporated-nickel devices without an applied voltage.

By increasing the distance of the electrodes, peaks compress and lengthen considerably for the transversal and longitudinal sweep, respectively, as Figure 4.9 shows.

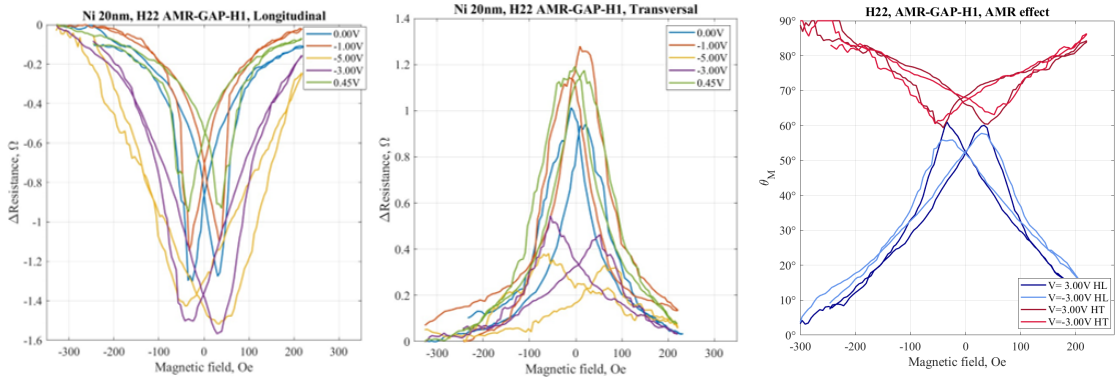

(a) **(b)** **(c)**

Figure 4.9: Longitudinal (a) and transverse (b) field sweeps for evaporated nickel with strip width equal to 1000nm and gap of 1300nm. (c) shows how the magnetization angle varies with the field.

Furthermore, the fact that voltages of opposite sign rotate the magnetisation by almost the same angle suggests a very symmetrical characteristic. If the thickness of the nanostrip is tripled to 3000nm, a worsening of the magnetoelectric effect can be seen in Figure 4.10.

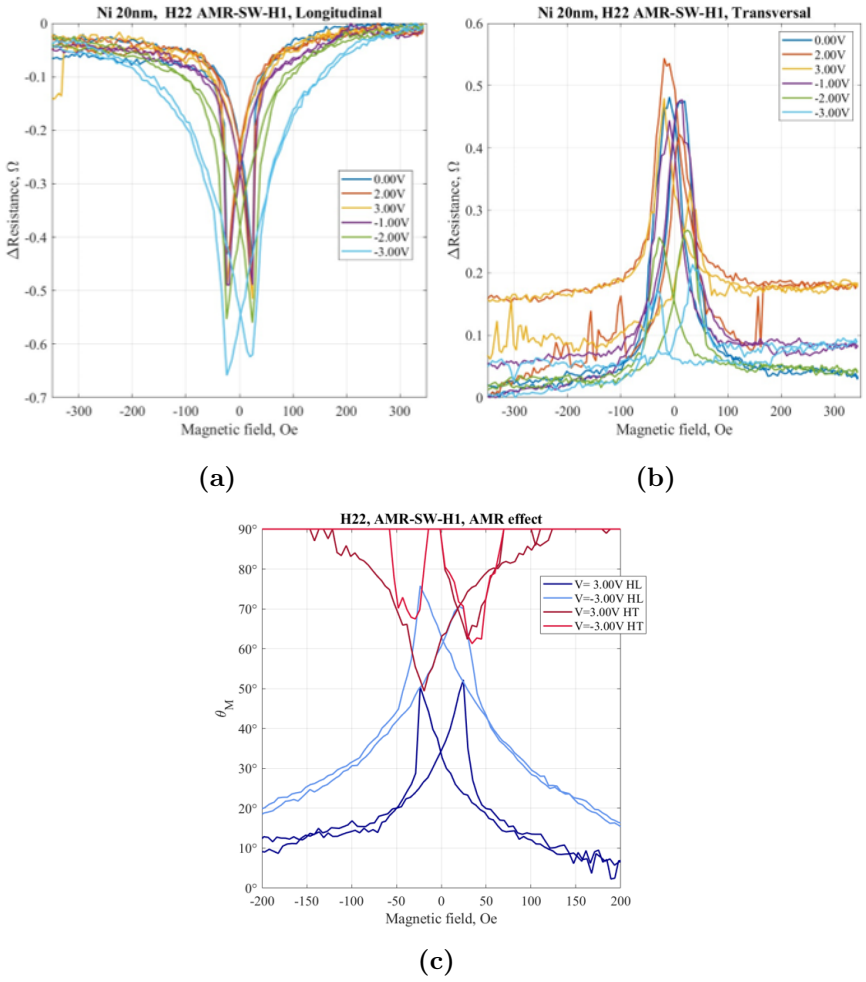

Figure 4.10: Longitudinal (a) and transverse (b) field sweeps for evaporated nickel with strip width equal to 3000nm and gap of 1000nm. (c) shows how the magnetization angle varies with the field.

4.3 Gate sweep results

BPZT, being ferroelectric, can exhibit two different strains for the same voltage, depending on the previous material state. To ensure consistency in the coupling measurement, it is therefore appropriate to get the BPZT in saturation so that the generated strain can be considered within the same arm of the ferroelectric hysteresis.

Starting the analysis in the same sequence as the field sweep measurements, it is evident that in the absence of a magnetic field, the applied voltage significantly alters the resistance. This change results in the clearly defined butterfly loop visible in the figure 4.11. The application of a magnetic field neutralizes the effects of the voltage, as the strain generated is insufficient to produce a magnetic field strong enough to counteract the influence of the external magnetic field. As a result, the impact of the voltage on resistance is significantly diminished. Moreover the curves

were obtained by positioning the device longitudinally therefore the application of the magnetic field maximizes the resistance.

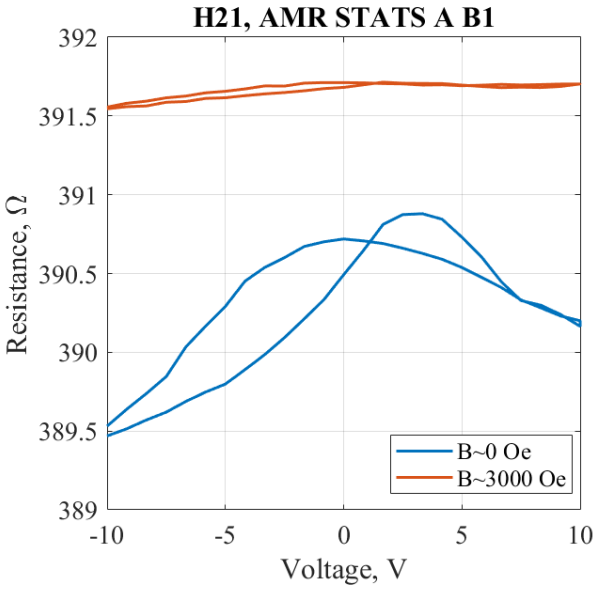

Figure 4.11: Gate sweep for sputtered nickel device with strip width equal to 1000nm and gap of 1000nm without applying any magnetic field (in blue) and with a magnetic field of $B = 3000Oe$ (in red)

Using equation 4.1, the butterfly loop can be expressed in terms of the magnetization angle, showing how different voltages alter this angle. However, it is important to note that the amplitude of the butterfly loop also depends on the initially applied voltage, which influences the overall magnetization behavior. Looking the minor loop in Figure 4.12, when an initial voltage of -5V is applied, the two curves are quite similar. The main differences become apparent when the voltage decreases after reaching 5V. In this case, the voltage has a reduced effect, resulting in weaker coupling.

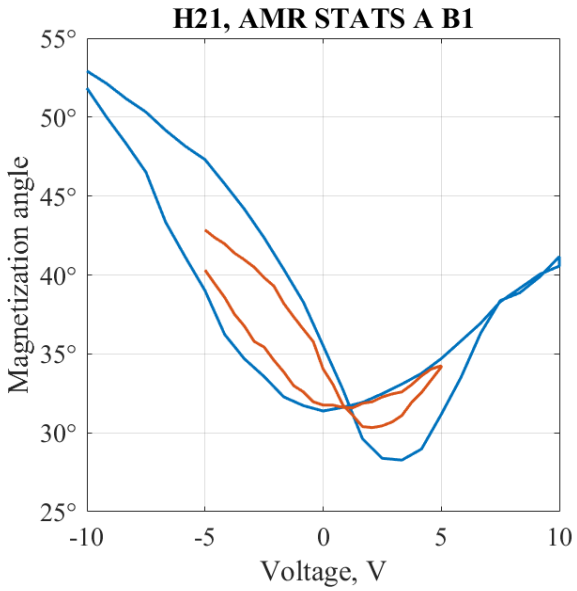

Figure 4.12: Magnetization angle versus voltage for two different loops. The minor loop (in red) was obtained by applying voltages between -5 V and 5 V

Being made of composite, studying the interaction between the two layers is very challenging. Consequently, to simplify the calculation of the magnetoelectric coupling coefficient, it is essential to ensure saturation. This allows the voltage-induced stress to be considered constant, thereby eliminating uncertainties related to the hysteresis of the ferroelectric layer. Starting from the formula 2.22, it is possible to make valid simplifications based on simulations. First of all from the simulations it has been seen how the shear strain components and ϵ_{xx} are negligible with respect all the others. Moreovoer the magnetization along the z-component is also negligible. For this reason 2.22 simplifies to:

$$H_{me} = -\frac{2}{\mu_0 M_s} \begin{pmatrix} 0 \\ B_1 m_y \epsilon_{yy} \\ 0 \end{pmatrix} \tag{4.2}$$

To calculate the coupling coefficient, it will be sufficient to take the derivative of H_{me} with respect to voltage. This can be done in *Matlab* using the same parameters as in the simulations and by expressing m_y in polar coordinates ($m_y = \sin\theta_M$). This leads to a maximum coupling α of 2.14 Oe/V for the positive voltages shown in Figure 4.13.

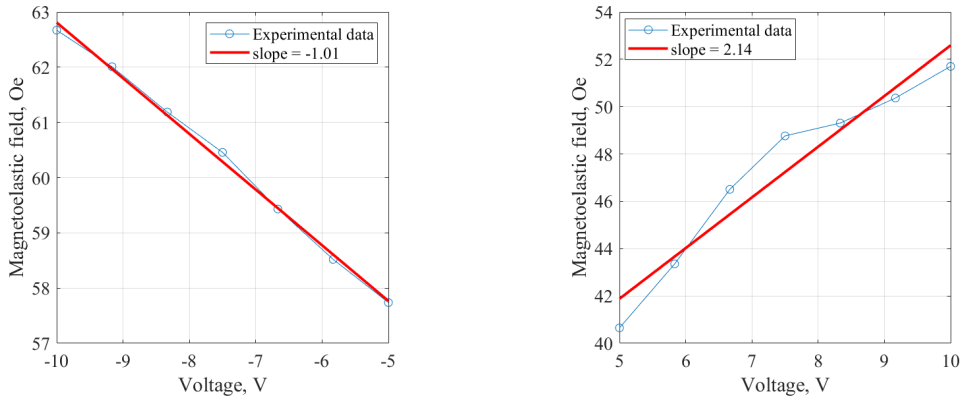

(a) **(b)**

Figure 4.13: H_{me} versus V for sputtered nickel device with strip width equal to 1000nm and gap of 1000nm

By reducing the gap distance instead, one can immediately notice a deterioration in the overall behaviour of the butterfly loop, which appears much more squashed and smaller in Figure 4.14b. This confirms the bad coupling if the electrodes are too close to the nanostrip.

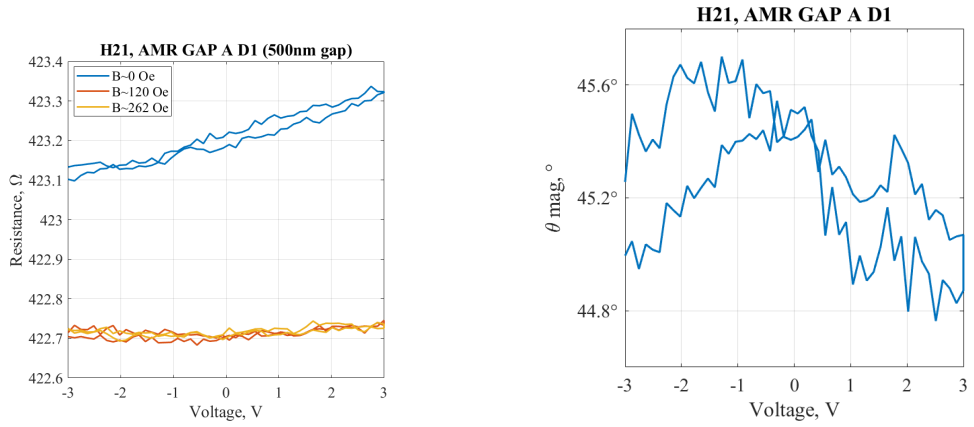

(a) **(b)**

Figure 4.14: Gate sweep measurements for sputtered nickel device with strip width equal to 1000nm and gap of 500nm with applying a transversal magnetic field and without (a). The magnetization angle versus the voltage is shown in (b)

Then, by reducing the strip width, it is noticeable that the butterfly loop once again exhibits a not optimal coupling as presented in Figure 4.15. While the performance is an improvement over the previously described case, achieving a maximum coupling of 0.7 Oe/V, it is still significantly weaker compared to the device with a width of one micrometer

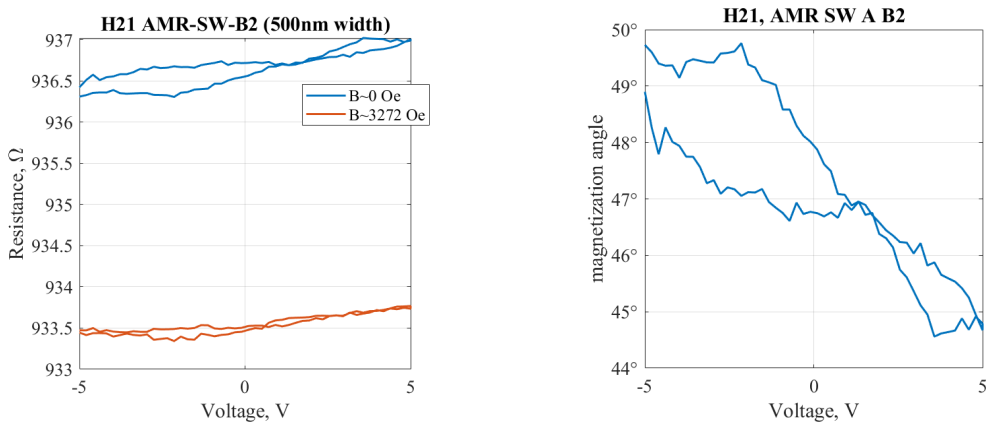

(a) (b)

Figure 4.15: Gate sweep measurements for sputtered nickel device with strip width equal to 500nm and gap of 1000nm with applying a transversal magnetic field and without (a). The magnetization angle versus the voltage is shown in (b)

The best characteristics were observed in devices with evaporated nickel. Specifically, in the case of the $1\mu m$ wide H22 STATS nanostrip, a distinct butterfly loop is clearly evident in Figure 4.16, and the minor loop corresponds closely to our initial observations.

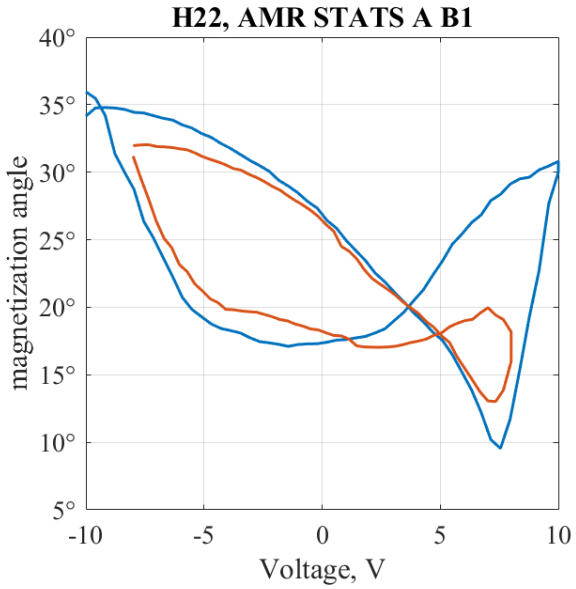

Figure 4.16: Gate sweep measurements for evaporated nickel device with strip width equal to 1000nm and gap of 1000nm

This correlation is further substantiated by the calculated coupling coefficient in Figure 4.17b, which peaks at a maximum value of 10 Oe/V for positive voltages.

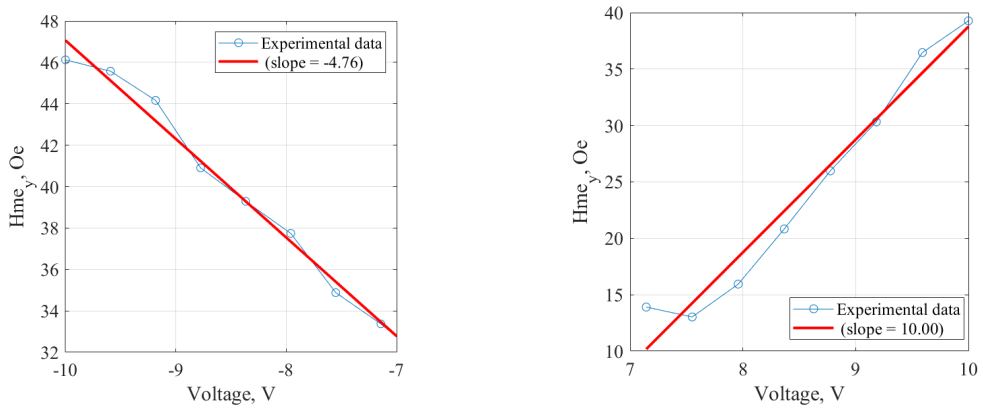

(a) **(b)**

Figure 4.17: H_{me} versus V for evaporated nickel device with strip width equal to 1000nm and gap of 1000nm

Increasing the electrode distance reveals that the device tolerates higher voltages less effectively (near 10 V, the device exhibits significant losses). However, the minor loop in Figure 4.18 shows a seemingly improved characteristic due to its high symmetry. Deriving the coupling yields a maximum value of 5 Oe/V.

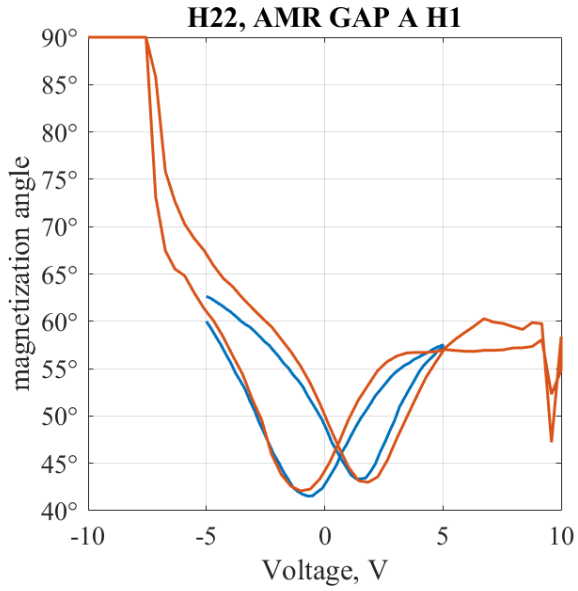

Figure 4.18: Gate sweep measurements for evaporated nickel device with strip width equal to 1000nm and gap of 1300nm

Increasing the thickness of the strip shows a deterioration in coupling. In fact, the graph shown in Figure 4.19 shows that when trying to apply more than 3V, the device no longer seems to work correctly, not showing a true butterfly loop. For negative voltages, however, a maximum coupling of 0.35 Oe/V can be assigned.

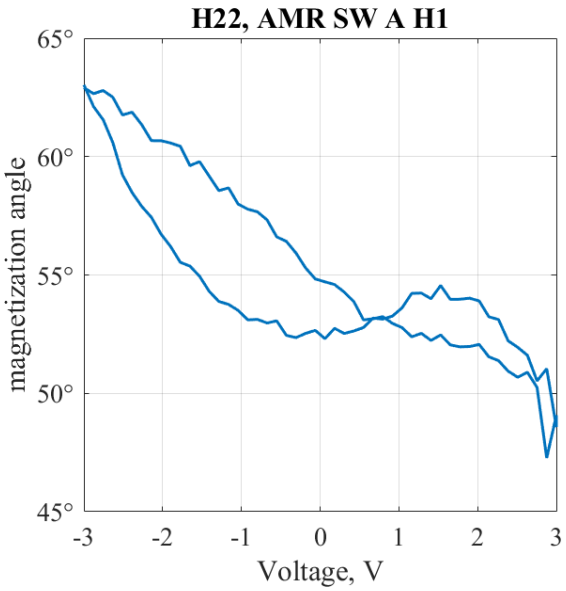

Figure 4.19: Gate sweep measurements for evaporated nickel device with strip width equal to 3000nm and gap of 1000nm

Chapter 5

Conclusion and outlook

5.1 Conclusion

In this presented thesis, some magnetoelectric device were studied in order to evaluate the magnetoelectric effect in thin-film composite made by BPZT/Ni using anisotropic magnetoresistance effect. The magnetoelectric coupling has been evaluated by measuring how the magnetization angle, related to a specific value of the resistance, changes depending on the voltage applied.

The first part of this thesis shows how the physics behind the magnetoelectric effect in thin films depends very much on the fabrication steps, the choice of materials and the geometry of the configuration used for measurements. Some multiphysics simulations were run to support this in order to examine the behavior of the BPZT/Ni composite devices in more detail. Electromechanical simulations were useful to study and understand the strain distribution in the magnetostrictive layer. Additionally, the simulations indicated that to maximize strain, the nanostrip should be $1\mu m$ wider and positioned $1\mu m$ away from the gate electrodes. Micromagnetic simulations were useful to show how different factors influence loop hysteresis, in particular how reducing the sample thickness leads to an increase in coercivity.

In the last part the devices were measured, doing different type of measurement. In the field sweep measurement both transversal and longitudinal hysteresis loops were studied for different voltages, thus analysing how the magnetoelastic field affects it. It was observed that devices made by evaporated-Nickel show a better butterfly loop and a smaller coercive field. In fact, this last property gives an indication of how soft the material is and thus how it reacts to small external stimuli.

The maximum coupling equal to 10 Oe/V has been obtained for the evaporated nickel device with the optimal width and gap distance as expected. In addition the most symmetric characteristic has been obtained for the evaporated nickel with a gap distance of 1300nm with the maximum coupling coefficient of 5 Oe/V. Furthermore, the butterfly loop of the sputtered Nickel is good but the coupling is five times smaller. The results of this study show that to achieve a better coupling using

thin films composite, it would be more appropriate to deposit a softer material using a gentle deposition technique. Furthermore, due to the geometry used in these devices, it is difficult to try to further reduce the size of the system, which would result in a smaller coupling.

5.2 Outlook

Although the magnetoelectric effect has been demonstrated in these composites, further research is needed to achieve sufficiently high magnetoelectric coupling coefficient for low-voltage or in logic devices. One aspect of this research is that there are many degrees of freedom, each of which could bring major improvements. The use of materials with a high magnetostrictive coefficient are the first solution to increase the coupling coefficient. New materials and alloys have been characterised in recent years. Among them, Galfenol Fe_xGa_{1-x} is very attractive in this field. Based on the stoichiometric ratio, one can manipulate the elastic and magnetic properties according to the desired purposes. Furthermore, by manipulating the geometry of the device, one could also try to use shear stress components to increase the contribution on the magnetoelastic field. This could be done by creating more complex three-dimensional structures made by using heterostructures [13]. The attempt to maximise stress transfer in each requires more research and more experimental measurements on different configurations. Finally, it should be noted that with the current state-of-art, it is possible to make a switch of up to 90°. Further research on how to make a 180° switch is needed for various applications such as in the MeRAMTJ [7].

Bibliography

[1] IEEE International Roadmap for Devices and Systems, "Executive Summary 2022." Institute of Electrical and Electronics Engineers, 2022, doi: 10.60627/C13Z-V363.

[2] IEEE International Roadmap for Devices and Systems, "Beyond CMOS and Emerging Materials Integration." Institute of Electrical and Electronics Engineers, 2023, doi: 10.60627/0P45-ZJ55.

[3] Wikipedia contributors. "Moore's law." Wikipedia, The Free Encyclopedia. Wikipedia, The Free Encyclopedia, 5 Jul. 2024. Web. 13 Jul. 2024.

[4] Bader, S.D., and S.S.P. Parkin. "Spintronics." Annual Review of Condensed Matter Physics 1, no. 1 (August 10, 2010): 71–88. https://doi.org/10.1146/annurev-conmatphys-070909-104123.

[5] Li, Hai, Dmitri E. Nikonov, Chia-Ching Lin, Kerem Camsari, Yu-Ching Liao, Chia-Sheng Hsu, Azad Naeemi, and Ian A. Young. "Physics-Based Models for Magneto-Electric Spin-Orbit Logic Circuits." IEEE Journal on Exploratory Solid-State Computational Devices and Circuits 8, no. 1 (June 2022): 10–18. https://doi.org/10.1109/JXCDC.2022.3143130.

[6] Hosur, Sujay, Rammohan Sriramdas, Sumanta Kumar Karan, Na Liu, Shashank Priya, and Mehdi Kiani. "A Comprehensive Study on Magnetoelectric Transducers for Wireless Power Transfer Using Low-Frequency Magnetic Fields." IEEE Transactions on Biomedical Circuits and Systems 15, no. 5 (October 2021): 1079–92. https://doi.org/10.1109/TBCAS.2021.3118981.

[7] Bibes, M., Barthélémy, A. "Towards a magnetoelectric memory." Nature Mater 7, 425–426 (2008). https://doi.org/10.1038/nmat2189

[8] Hu, Jia-Mian, Ce-Wen Nan, "Opportunities and Challenges for Magnetoelectric Devices." APL Materials 7, no. 8 (August 1, 2019): 080905. https://doi.org/10.1063/1.5112089.

[9] Qiao, Huimin, Chenxi Wang, Woo Seok Choi, Min Hyuk Park, and Yunseok Kim. "Ultra-Thin Ferroelectrics." Materials Science and Engineering: R: Reports 145 (July 2021): 100622. https://doi.org/10.1016/j.mser.2021.100622.

[10] Spaldin, N. A., and R. Ramesh. "Advances in Magnetoelectric Multiferroics." Nature Materials 18, no. 3 (March 2019): 203–12. https://doi.org/10.1038/s41563-018-0275-2.

[11] Chen, Aitian, Hong-Guang Piao, Minhui Ji, Bin Fang, Yan Wen, Yinchang Ma, Peisen Li, and Xi-Xiang Zhang. "Using Dipole Interaction to Achieve Nonvolatile Voltage Control of Magnetism in Multiferroic Heterostructures." Advanced Materials 33, no. 52 (December 2021): 2105902. https://doi.org/10.1002/adma.202105902.

[12] Vaz, Carlos A. F., Jason Hoffman, Charles H. Ahn, and Ramamoorthy Ramesh. "Magnetoelectric Coupling Effects in Multiferroic Complex Oxide Composite Structures." Advanced Materials 22, no. 26–27 (July 20, 2010): 2900–2918. https://doi.org/10.1002/adma.200904326.

[13] He, Wei. "A Shear-Mode Magnetoelectric Heterostructure with Enhanced Magnetoelectric Response for Stray Power-Frequency Magnetic Field Energy Harvesting." Micromachines 13, no. 11 (November 1, 2022): 1882. https://doi.org/10.3390/mi13111882.

[14] A. P. Guimarães. Priniples of Nanomagnetism. NanoScience and Technology. Springer Berlin, Heidelberg, 2009. ISBN 978-3-642-26111-4.

[15] R.C. O'Handley, Magnetic Materials, Robert A. Meyers, Encyclopedia of Physical Science and Technology (Third Edition), Academic Press, 2003, Pages 919-944, ISBN 9780122274107.

[16] Wikipedia contributors. (2023, January 29). Zeeman energy. In Wikipedia, The Free Encyclopedia. Retrieved 19:12, July 8, 2024, from *https* : *//en.wikipedia.org/w/index.php?title* = *Zeeman_energy*&*oldid* = 1136237604

[17] B. Doudin, J.P. Ansermet, Nanostructuring Materials for Spin Electronics, Europhysics news, 1997, doi: 10.1007/s00770-997-0014-8

[18] T. McGuire and R. Potter, "Anisotropic magnetoresistance in ferromagnetic 3d alloys," IEEE Trans. Magn., vol. 11, no. 4, pp. 1018–1038, Jul. 1975, doi: 10.1109/TMAG.1975.1058782.

[19] J. Holanda, D. S. Maior, A. Azevedo, and S. M. Rezende, "Anisotropic magnetoresistance and anomalous Nernst effect in exchange biased permalloy/(1 0 0) NiO single-crystal," J. Magn. Magn. Mater., vol. 432, pp. 507–510, Jun. 2017, doi: 10.1016/j.jmmm.2017.02.038.

[20] Ye Jun, He Wei, Wu Qiong, Liu Haoliang, Zhang Xiang-Qun, Chen Ziyu, Cheng Zhao-Hua, Determination of magnetic anisotropy constants in Fe ultrathin film on vicinal Si(111) by anisotropic magnetoresistance, Scientific reports, 2013,doi: 10.1038/srep02148.

[21] P. Goodman, "Current and future uses of gold in electronics," Gold Bull., vol. 35, no. 1, pp. 21–26, Mar. 2002, doi: 10.1007/BF03214833.

[22] M. M. Vopson, Y. K. Fetisov, G. Caruntu, and G. Srinivasan, "Measurement Techniques of the Magneto-Electric Coupling in Multiferroics," Materials, vol. 10, no. 8, p. 963, Aug. 2017, doi: 10.3390/ma10080963.

[23] Getzlaff, Mathias. "Fundamentals of Magnetism", Berlin, New York, Springer, 2008.

[24] F. Luciano et al., "Microwave Properties of Ba-Substituted Pb(Zr 0.52 Ti 0.48)O 3 after Chemical Mechanical Polishing," ECS J. Solid State Sci. Technol., vol. 12, no. 9, p. 094006, Sep. 2023, doi: 10.1149/2162-8777/acf4bb.

[25] Bhaskar, U. K., D. Tierno, G. Talmelli, F. Ciubotaru, C. Adelmann, and T. Devolder. "BPZT HBARs for Magnetoelastic Stress Generation at GHz Frequencies." IEEE Transactions on Ultrasonics, Ferroelectrics, and Frequency Control 67, no. 6 (June 2020): 1284–90. https://doi.org/10.1109/TUFFC.2020.2967902.

[26] Budhathoki et al., "Low Gilbert damping and linewidth in magnetostrictive FeGa thin films," J. Magn. Magn. Mater., vol. 496, p. 165906, Feb. 2020, doi: 10.1016/j.jmmm.2019.165906.

[27] A. Nicolenco, Y. Chen, N. Tsyntsaru, H. Cesiulis, E. Pellicer, and J. Sort, "Mechanical, magnetic and magnetostrictive properties of porous Fe-Ga films prepared by electrodeposition," Mater. Des., vol. 208, p. 109915, Oct. 2021, doi: 10.1016/j.matdes.2021.109915.

[28] D. Narducci et al., "Magnetoelectric coupling in Ba:Pb(Zr,Ti)O3/Co40Fe40B20 nanoscale waveguides studied by propagating spin-wave spectroscopy," Appl. Phys. Lett., vol. 124, no. 18, p. 182408, Apr. 2024, doi: 10.1063/5.0198501.

[29] Joos, Jonas J., Pedram Bassirian, Pieter Gypens, Jeroen Mulkers, Kai Litzius, Bartel Van Waeyenberge, and Jonathan Leliaert. "Tutorial: Simulating Modern Magnetic Material Systems in Mumax3." Journal of Applied Physics 134, no. 17 (November 7, 2023): 171101. https://doi.org/10.1063/5.0160988.

[30] Wikipedia contributors. (2024, April 17). COMSOL Multiphysics. In Wikipedia, The Free Encyclopedia. Retrieved 16:21, July 11, 2024, from *https* : *//en.wikipedia.org/w/index.php?title* = *COMSOL_Multiphysics&oldid* = 1219364978

[31] B. D. Cullity and C. D. Graham, Introduction to Magnetic Materials, 1st ed. Wiley, 2008. doi: 10.1002/9780470386323.

[32] Wang Z, Zhang Y, Wang Y, Li Y, Luo H, Li J, Viehland D. Magnetoelectric assisted 180° magnetization switching for electric field addressable writing in

magnetoresistive random-access memory. ACS Nano. 2014 Aug 26;8(8):7793-800. doi: 10.1021/nn503369y. Epub 2014 Aug 7. PMID: 25093903.